ION SELECTIVITY AND GATING IN THE NAK CHANNEL

APPROVED BY SUPERVISORY COMMITTEE

Youxing Jiang, Ph.D

Johann Deisenhofer, Ph.D

Donald Hilgemann, Ph.D

Jose Rizo-Rey, Ph.D

DEDICATION

Dedicated to my parents, Drs. Seemeen and Anis Alam, and siblings Hina and Humr Alam, for their continued love and support. I also wish to thank members of my Graduate Committee, and numerous friends and colleagues who have been an integral part of graduate school and life in Dallas.

ION SELECTIVITY AND GATING IN THE NAK CHANNEL

by

AMER ALAM

DISSERTATION / THESIS

Presented to the Faculty of the Graduate School of Biomedical Sciences

The University of Texas Southwestern Medical Center at Dallas

In Partial Fulfillment of the Requirements

For the Degree of

DOCTOR OF PHILOSOPHY

The University of Texas Southwestern Medical Center at Dallas

Dallas, Texas

April, 2009

ION SELECTIVITY AND GATING IN THE NAK CHANNEL

AMER ALAM

The University of Texas Southwestern Medical Center at Dallas, 2009

YOUXING JIANG, Ph.D.

Ion selectivity and gating are two fundamental properties central to proper physiological functioning of ion channels. In this work, a thorough structural characterization of ion binding profiles is presented for the NaK channel, a non selective cation channel from *Bacillus cereus*, along with an analysis of channel opening and closing mechanisms. An introduction to the overall structure of the full length channel is presented along with initial characterization of its ion selectivity properties. The body of the thesis encompasses a detailed analysis of Ca^{2+} binding within NaK, followed by additional gating and selectivity studies using high resolution structures of a truncated form of the channel. Two Ca^{2+} binding sites are observed, both utilizing a unique Ca^{2+} chelation chemistry involving only backbone carbonyl groups as ligands, with Ca^{2+}

selectivity at the extracellular site mediated by a through space interaction with a conserved acidic residue, Asp66, seen in other Ca^{2+} conducting channels. In the high resolution structure of the truncated NaK channel, we observe the intracellular gate in an open conformation much like that seen in MthK, making NaK the first channel for which both open and closed state structures are known. This is combined with a structural analysis of ion binding within the NaK selectivity filter, which reveals several interesting features that shed light on the possible underlying mechanisms of ion non-selectivity.

TABLE OF CONTENTS

PRIOR PUBLICATIONS

Dulubova I, Lou X, Lu J, Huryeva I, Alam A, Schneggenburger R, Südhof TC, Rizo. EMBO A Munc13/RIM/Rab3 tripartite complex: from priming to plasticity? *J. 2005 Aug 17;24(16):2839-50. Epub 2005 Jul 28.*

Shi N, Ye S, Alam A, Chen L, Jiang Y. Atomic structure of a Na+- and K+-conducting channel. *Nature. 2006 Mar 23;440(7083):570-4. Epub 2006 Feb 8.*

Alam A, Shi N, Jiang Y. Structural insight into Ca2+ specificity in tetrameric cation channels. *Proc Natl Acad Sci U S A. 2007 Sep 25;104(39):15334-9. Epub 2007 Sep 18.*

Alam A, Jiang Y. Structural analysis of ion selectivity in the NaK channel. *Nat Struct Mol Biol. 2009 Jan;16(1):35-41. Epub 2008 Dec 21*

Alam A, Jiang Y. High-resolution structure of the open NaK channel. *Nat Struct Mol Biol. 2009 Jan;16(1):30-4. Epub 2008 Dec 21*

LIST OF FIGURES

LIST OF TABLES

CHAPTER ONE

Introduction

Ion channels represent a physiologically essential class of proteins that are ubiquitously expressed in organisms ranging from single celled bacteria to human beings[1]. These proteins reside within cell membranes, lipid bilayers approximately 40Å thick that surround individual cells or compartments within a cell, providing a barrier to the passage of components central to countless physiological processes. The oily nature of the membranes ensures that ions preferentially remain in the watery environment surrounding either side of the membrane, taking advantage of the electrically favorable interactions arising from the polarizable nature of water molecules. However, the passage of ions across these membranes is a prerequisite for vital processes such as the excitation of nerve and muscle cells. To this end, ion channels play a vital role by providing passageways, the ion conduction pores, within membranes to allow ions to traverse down their concentration gradients[1]. A simplistic representation of an ion channel is shown in figure 1.1, highlighting two fundamental properties that allow it to function optimally: channel gating and ion selectivity. Channel gating refers to the ability of ion channels to open and close their conduction pores in response to external stimuli such as changes in voltage or binding of ligands. These changes are sensed by different channel domains that usually undergo structural rearrangements coupled to pore opening or closing. Selectivity, on the other hand,

refers solely to the ability of ion channels to discriminate between different types of ions. This is usually a direct consequence of the unique structural and chemical environment within part of the ion channel pore, the selectivity filter, of different channels. Our understanding of both these processes has come a long way with the advancement of genetic, biochemical, and electrophysiological analysis of ion channels, and more recently the structural characterization of several of them[2-11]. I will focus mainly on advances in channel biology beginning with the structural characterization of K^+ selective channels, namely the groundbreaking work of Roderick Mackinnon and his colleagues in determining the first crystal structure of an ion channel, and subsequent studies on channel gating and selectivity of which the research presented here is an integral part of[9,10,12-15].

This document will provide basic background into the fundamental properties of members of the tetrameric cation channels, the largest family of ion channels which includes both cation selective and non selective channels. In these channels, four membrane spanning subunits units are arranged symmetrically around a central ion conduction pore through which specific ions can pass[16]. This introduction will lead directly into a basic discussion of the NaK channel, a non-selective prokaryotic channel discovered in our lab[5] and the focus of this thesis project.

Tetrameric Cation Channels: Basic Pore Properties

Regardless of their ion selectivity properties, the overall architecture of the pore region of tetrameric cation channels is thought to be highly conserved among different members of the family. Figure 1.2 shows a sequence alignment of several tetrameric cation channel pores highlighting conserved secondary structure elements, namely the inner, outer, and pore helices, as well as the selectivity filter. As can be seen, the pore region comprises two transmembrane helices, the inner and outer helices separated by a loop region, known as the p-loop or re-entrant loop, containing an additional pore helix as well as the selectivity filter. The structure determination of KcsA, a prototypical K^+ channel, revealed the overall arrangement of these different structural elements in tetrameric cation channels[12]. The overall structure, presented in figure 1.4, reveals an 'inverted teepee' shaped pore. The four monomers are arranged in a four fold symmetric fashion about the ion conduction pathway. The pore helices are arranged so as to point their C-termini towards the central cavity, where they are thought to stabilize a hydrated K^+ ion[12,13]. The selectivity filter of the channel forms the narrowest part of the pore where ions pass in a single file as had been predicted previously. Furthermore, the structure of the KcsA selectivity filter confirmed earlier predictions that only dehydrated ions could traverse its length as discussed in further detail below.

Ion Selectivity in the Tetrameric Cation Channel Pore.

Ion selectivity studies of tetrameric cation channels have predominantly focused on the issue of K^+ over Na^+ selectivity. Namely, how does an ion channel allow K^+ ions to pass through their pores at near diffusion limited rates while almost completely excluding the smaller Na^+ ions? The model that dominated the field over the last few decades is the so called snug-fit model, summarized in figure 1.3. It suggested the presence of a filter region, later characterized as the selectivity filter, which is optimized to bind dehydrated K^+ ions but not Na^+ ions. Consequently, the energetic cost of K^+ ions entering the selectivity filter in a dehydrated state is much lower than that of Na^+ ions, allowing K^+ channels to maintain a high level of K^+ over Na^+ selectivity. Subsequent mutagenesis studies further confirmed the existence of the selectivity filter, identifying its sequence as TVGYG, the so called signature sequence, which is very highly conserved in all K^+ channels[17-19]. The sequence alignment of the filter region of different K^+ channels as well as Na^+, Ca^{2+}, and non selective channels like the Cyclic Nucleotide Gated (CNG) channels highlights the conservation of signature sequences within different sets of tetrameric cation channels. Subtle differences in the K^+ channel signature sequence can lead to drastic changes in ion selectivity.

The crystal structure of KcsA provided a first glimpse at the structural and chemical environment within the selectivity filter of a K^+ channel. As shown in Figure 1.5, the K^+ channel selectivity filter contains four K^+ binding sites formed

by the backbone carbonyl groups of the signature sequence amino acids along with the side-chain hydroxyl group of Thr75. Additionally, the structure showed a hydrated K^+ ion in the water filled cavity intracellular to the selectivity filter. The ligand(oxygen atoms)-ion distances for ions in the selectivity filter of K^+ ions are very similar to the ion-oxygen (from water molecules) distances for the ion in the cavity. In effect, the chemical environment of the four K^+ binding sites in the selectivity filter mimics the hydration state (assuming an octahedral arrangement of ligands) of K^+ ions in bulk solution. Even though the hydration state of K^+ ions in solution is a topic of some debate, the observation of an octahedral ligand chemistry for hydrated K^+ ions in the cavity has been seen in numerous crystal structures of K^+ channels as will be discussed in more detail in chapter 4. In order to enter the selectivity filter, a K^+ ion would have to shed eight water molecules. The ligand arrangement in the selectivity filter compensates in part for the energetic cost of this process. The same does not hold true for hydrated Na^+ ions as the K^+ selective filter is not optimized for Na^+ binding, presumably endowing the channel high K^+ over Na^+ selectivity.

Gating in Tetrameric Cation Channels.

In order for ion channels to function properly, the opening and closing of the channel pore has to be tightly controlled. Most channels can be classified in terms of their gating mechanisms. The large family of voltage gated ion channels includes voltage gated K^+, Na^+, and Ca^{2+} channels. These are primarily

responsible for the generation of nerve impulses in excitable cells. A detailed description of voltage sensing in tetrameric cation channels is beyond the scope of this thesis. In short, the voltage sensing domain located in the S4 transmembrane segment senses changes in voltage, inducing a conformational change that is coupled to pore opening.

Ligand gated ion channels contain ligand binding domains attached to the channel pore via flexible linkers. Like voltage gated ion channels, ligand binding induces conformational changes in the ligand binding domain which are coupled to pore opening. No matter what the mechanism of gating, the end result is the opening or closing of the channel pore. So far, our knowledge of the open and closed state structures of tetrameric cation channels comes from different of various K^+ like KcsA, MthK, and ligand gated K^+ channels. The overall characteristics of the KcsA structure have already been described. The observation of straight inner helices and the resulting bundle crossing has led to the proposal that this structure is in a closed state. The MthK structure, on the other hand, revealed inner helices that were bent at a conserved glycine residue, known as the gating hinge. Consequently, the pore opening seen in the MthK structure is much wider than that in KcsA and this structure was therefore proposed to represent the open state of tetrameric cation channels. No matter what the underlying mechanisms involved are, it is generally accepted that the gating

state transition in tetrameric cation channels entail structural changes switching the pore between the two conformations seen in KcsA and MthK.

The NaK Channel

Until recently, efforts to elucidate the structural basis for cation channel selectivity and gating have focused mainly on crystal structures of various K^+ channels. All these structures have one thing in common: an identical selectivity filter. Even though the mechanisms underlying K^+ selectivity are well understood, there nevertheless remains a shortage of structures of non K^+ selective selectivity filters. To this end, the work presented in this thesis, namely the structural and functional characterization of the non selective bacterial channel NaK, presents a fundamental advance in the field of ion channel biology especially in respect to selectivity. My involvement in this project initially started with determining the ion selectivity properties of the NaK channel, which I will present as introductory material along with the initial structural characterization of NaK done in our lab. NaK, a member of the tetrameric cation channel family bearing strong sequence similarities with KcsA, was identified in our laboratory after a screen of the bacterial genome in search for channels carrying the TVGYG signature sequence or variations of it. As shown in figure 1.2, the NaK selectivity filter sequence strongly resembles that of KcsA except for a key residue position which is occupied by Tyr in KcsA but Asp in NaK, equivalent to Cyclic Nucleotide Gated (CNG) channels, where the equivalent position is also occupied by an acidic

residue. This suggested that NaK and CNG channels could share structural similarities in the selectivity filter region and therefore similar ion selectivity properties. Our initial functional characterization of NaK strongly supported this hypothesis, as described below, and the structure of the NaK selectivity filter revealed interesting features that likely underlie the channel's non selective nature.

Na^+ and K^+ complex structures of the NaK channel

All initial structural work on the NaK channel was performed by Dr. Ning Shi in our lab and therefore only a discussion of the results will be presented here. The overall structure of NaK in complex with Na^+ at a resolution of 2.4A is shown in figure 1.6. The structure, reminiscent of KcsA in terms of overall architecture, shows a channel pore consisting of four subunits arranged in a four fold symmetric fashion about a central ion conduction pore. Like KcsA, each NaK subunit comprises the outer and inner transmembrane helices, labeled M1 and M2, joined by a reentrant loop containing the pore helices (P) as well as the selectivity filter residues. Unlike the KcsA structure however, NaK contains an interfacial N-terminal helix, M0, positioned parallel to the membrane plane and a likely mediator of inner helix opening or closing. As discussed below, the removal of this helix does indeed cause an increase in ion flux through the NaK channel, be it because of an increase in open probability, conductance, or both.

What sets NaK apart from K^+ channels, however, is the structure of its selectivity filter. Figure 1.7 presents a comparison of the NaK selectivity filter and that of KcsA. As discussed previously, the K^+ channel selectivity filters all contain four K^+ binding sites

that are roughly chemically equivalent, allowing for rapid and selective conductance of K^+ ions. The NaK selectivity filter, however, preserves only two of these sites, labeled 3 and 4 for comparison. Sites 1 and 2 are replaced by a vestibular structure where ions are still seen to bind, albeit more diffusely.

Initial characterization of ion selectivity in the NaK channel.

A considerable amount of information regarding the mechanisms underlying K^+ selectivity has been gathered over the past decade with the structure determination of several K^+ channels[1,2,7-12,20-27]. The K^+ channel selectivity filter has been used as a structural model to probe selectivity properties in both selective and non-selective cation channels. NaK therefore presented an attractive opportunity to visualize a selectivity filter different than that of K^+ channels. Functional characterization of the channel using electrophysiological tools proved difficult owing possibly to an inherently low open probability and/or conductance rate. As an alternative, we employed a radioactive uptake assay utilizing ^{86}Rb as a tracer. In short, the NaK channel was over-expressed and purified from *E.coli* Xl1 Blue cells by extraction from the cell lysate using the detergent decyl maltoside (DM). Purified protein was incubated with detergent solubilized lipid (3:1 ratio of POPE:POPG) in the presence of 400-450mM XCl (X= monovalent cation). Proteoliposomes were formed by slowly dialyzing away the detergent. Upon exchange the liposomes, containing 450mM XCl inside, into a low salt buffer a concentration gradient of ion X is formed driving the outflow of X^+ into to the extraliposomal medium. This in turn initiates a buildup of excess negative charge inside the liposome, driving the influx of any trace amounts of ^{86}Rb introduced into the extralipsomal solution after the buffer exchange step. Upon elimination of extraliposomal ^{86}Rb, the radioactivity levels

inside liposomes can be counted at different time points. As shown in Figure 8, a time dependent increase in ^{86}Rb levels is seen for liposomes loaded with both Na^+ and K^+, indicating that the channel conducts both ion species. Also shown are the results of competition assays where additional cations are added to the extraliposomal mix in addition to ^{86}Rb and the change in time dependent ^{86}Rb influx in liposomes is analyzed. In the presence of externally added Na^+ or K^+, ^{86}Rb influx is seen to decrease, further confirming that NaK conducts both ions which 'compete' with ^{86}Rb for entry into liposomes. This effect is not seen in the presence of externally added Li^+, or NMG.

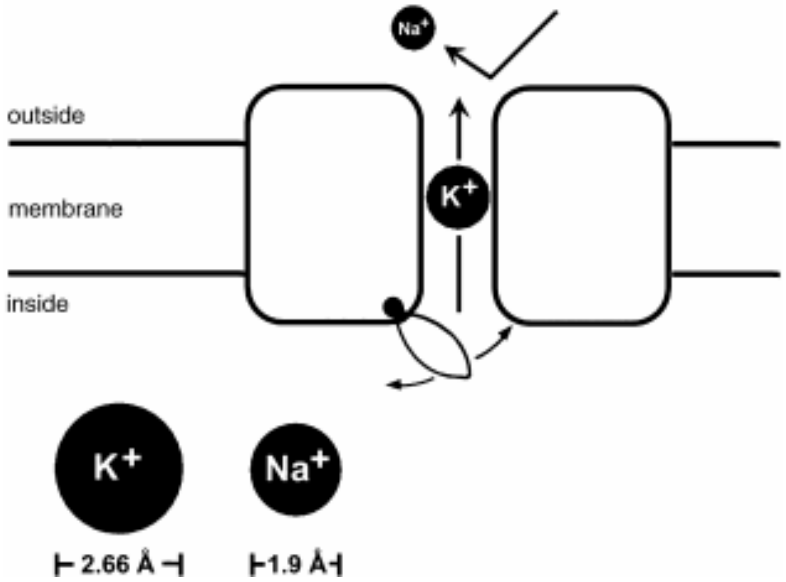

R. Mackinnon, *Nobel Lecture*

Figure 1.1 Simplistic representation of an ion channel. The two fundamental ion channel properties, selectivity and gating, are highlighted by a K+ selective pore and the C-terminal 'gate', respectively.

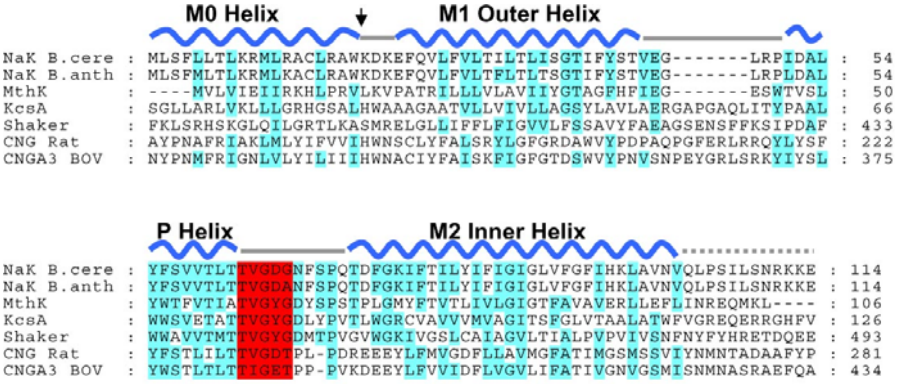

Figure 1.2 Sequence alignment of several tetrameric cation channels, including K+ selective channels, and two groups of non-selective channels: the non-selective Cyclic Nucleotide Gated (CNG) channels, and the bacterial NaK channels.

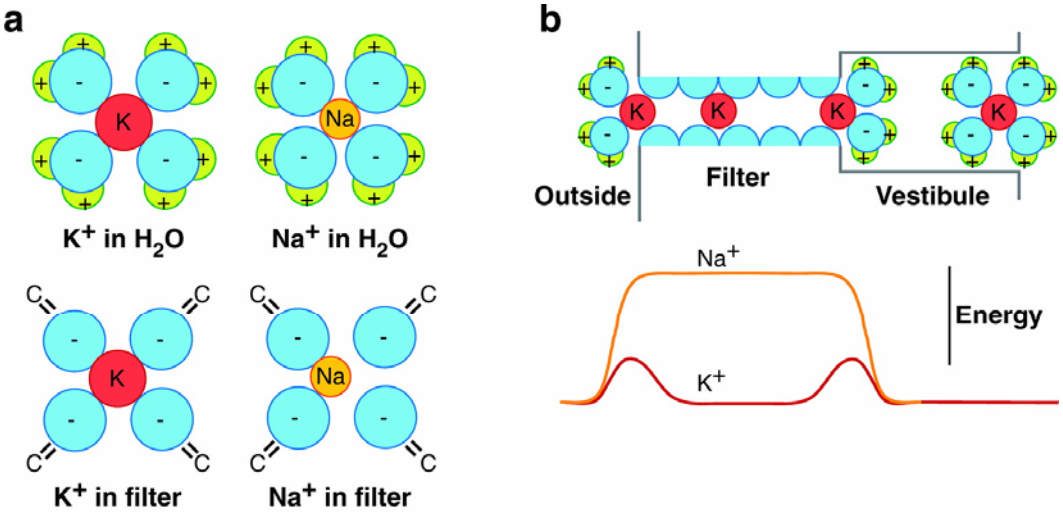

Armstrong CM. 2007.
Annu. Rev. Physiol. 69:1–18

Figure 1.3 The 'Snug-Fit Model. a) K^+ and Na^+ ions (red and orange spheres, respectively) shown in a hydrated (upper) and within the selectivity filter of a K+ channel to demonstrate the proposed optimal binding of K^+ but not Na^+. b) Representation of K+ dehydrated K+ ions entereing the selectivity filter in single file (upper) and a representation of increased energetic cost of dehydrating Na^+ ions in order to enter the same filter compared to K^+ (lower)

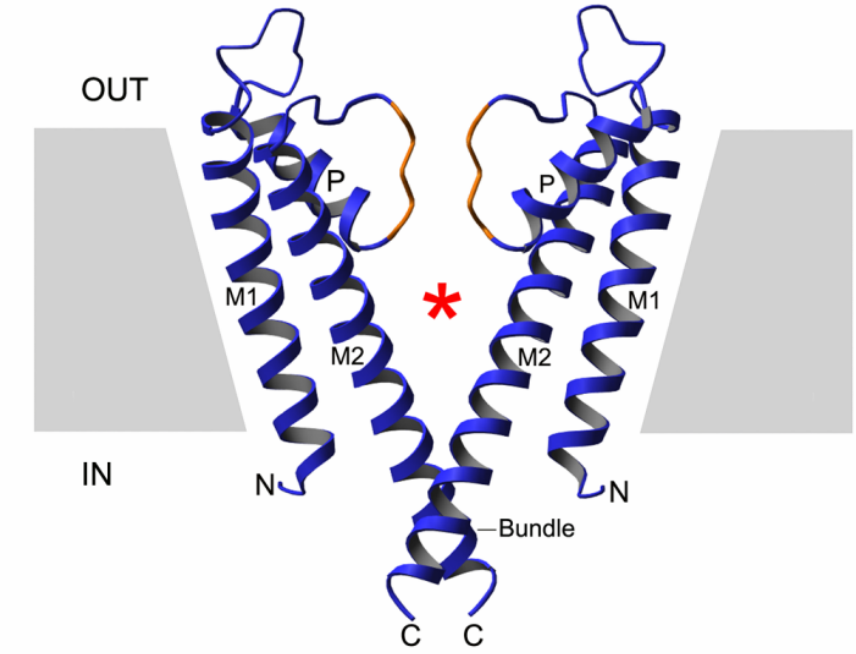

Figure 1.4 Overall structure of the KcsA K+ channel with proximal and distal subunits removed for clarity. The star denotes the central water filled cavity. Outer, inner, and Pore helices are labeled M1, M2, and P, respectively and the C-terminal bundle crossing formed by the inner helices is also highlighted. Residues comprising the selectivity filter are colored orange.

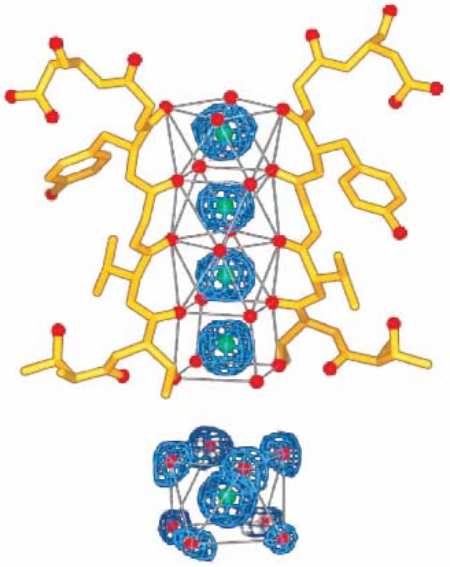

Figure 1.5 The selectivity filter of KcsA. Four K+ binding sites are shown, each displaying an octahedral ligand chemistry mimicking the hydration shell seen for the ion in the central cavity

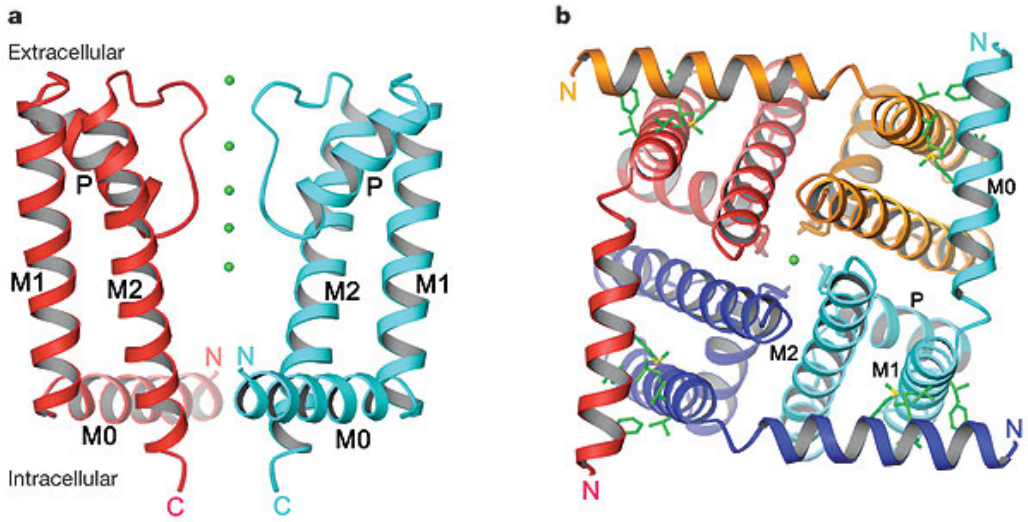

Figure 1.6 Ribbon representation of NaK viewed from the membrane in **a** (with front and rear subunits removed), and from the intracellular side in **b**. Green spheres represent ions in the channel. Each subunit is individually coloured. Green ball-and-stick representations show side chains from residues involved in hydrophobic contacts between M0 and neighbouring M1 helices.Overall structure of the NaK channel viewed from the membrane plane with proximal and distal subunits removed (**a)** and the intracellular side. M0, M1, M2, and P represent the N-terminal cytoplasmic helix, the outer, inner, and pore helices, respectively (Shi et. al[5])

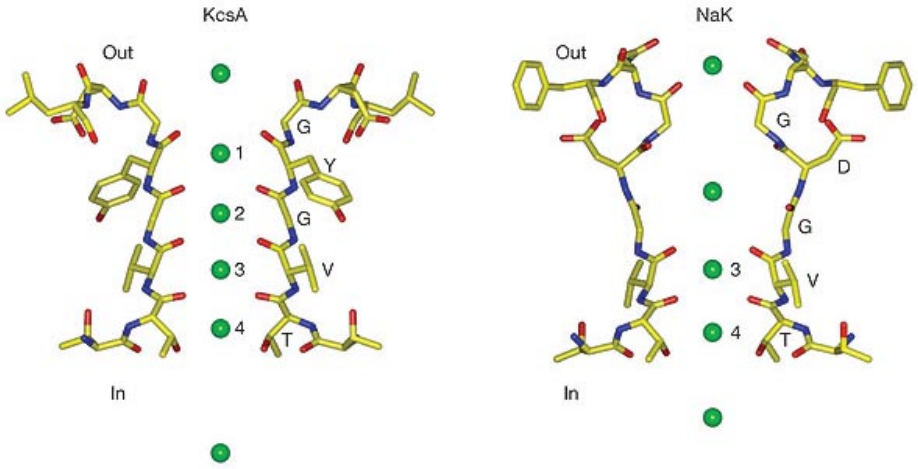

Figure 1.7 Structural details of the selectivity filters from KcsA (left) and NaK (right)[5]. The front and rear subunits have been removed for clarity. Only discrete ion-binding sites in the filter are numbered (1–4 from the extracellular side in KcsA, 3 and 4 in NaK).

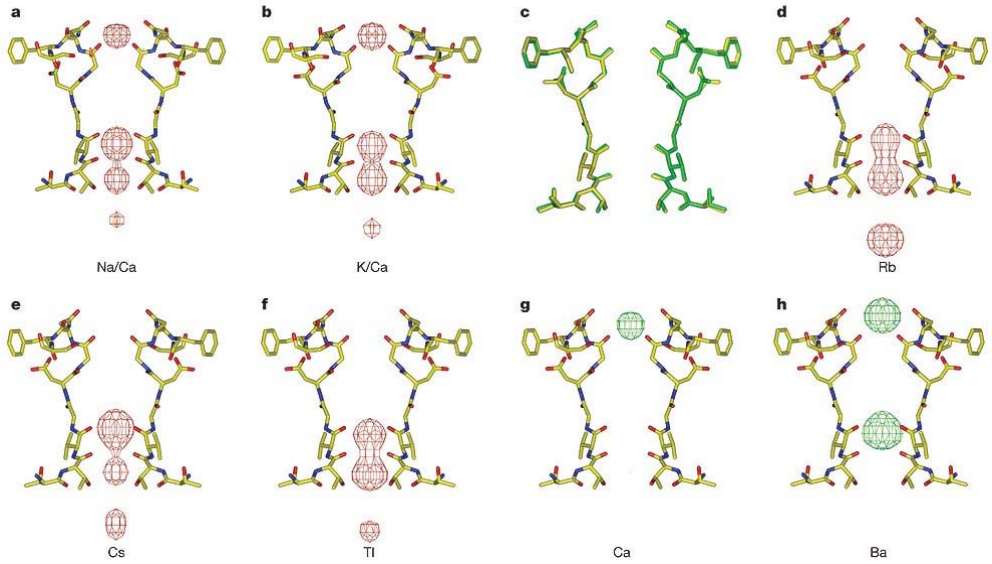

Figure 1.8 a, b, $2F_o–F_c$ ion-omit maps of Na^+ (a) and K^+ (b) complexes of NaK contoured at 6σ (red mesh). c, Superimposition of NaK selectivity filters in Na^+- (green) and K^+- (yellow) bound states. **d–h**, $F_{soak}–F_{reference}$ difference maps between the reference crystal and crystals with various soaking conditions reveal the binding of cations (labelled underneath each panel) in NaK. All maps are contoured at 10σ except for the density of Ca^{2+} binding, which is contoured at 6σ. Densities for monovalent and divalent cations are coloured red and green, respectively.

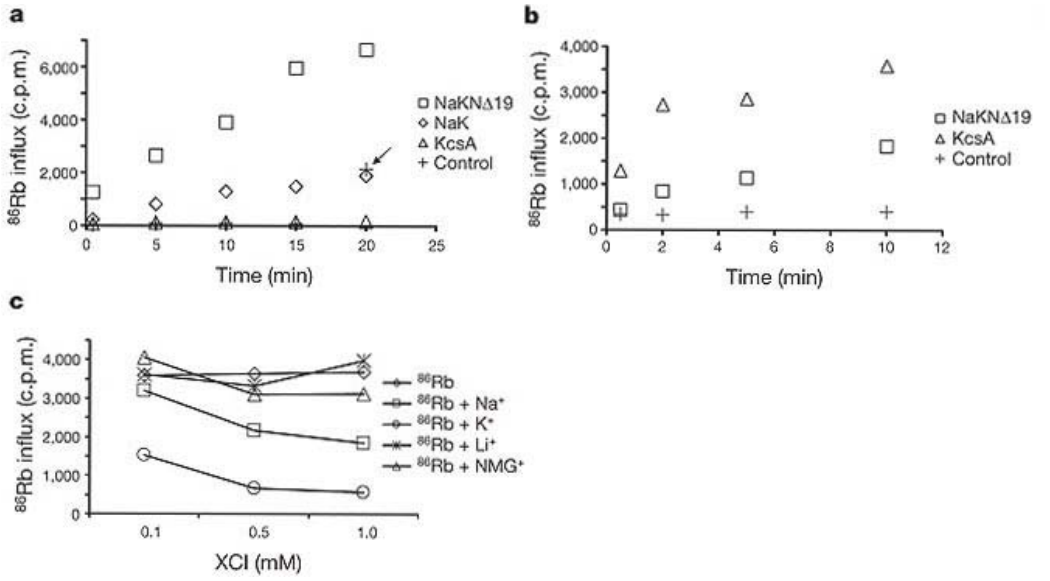

Figure 1.9[5]. a, Time-dependent ^{86}Rb influx into liposomes prepared in NaCl. The liposomes contain NaK, NaKNΔ19, KcsA or no protein (as a control). Arrow indicates ^{86}Rb influx into control liposomes upon addition of 10 μg ml^{-1} gramicidin A. **b**, Time-dependent ^{86}Rb influx into KcsA or NaKNΔ19-containing liposomes prepared in KCl. **c**, Competition assay showing ^{86}Rb influx in the presence of externally added monovalent cations. Three final concentrations of each cation (0.1, 0.5 and 1.0 mM) were tested in the assay. No external cations were added in the control experiment. c.p.m., counts per minute.

CHAPTER 2

Structural Insight into Ca^{2+} Specificity in Tetrameric Cation Channels.

Abstract

Apparent blockage of monovalent cation currents by the permeating blocker Ca^{2+} is a physiologically essential phenomenon relevant to Cyclic-Nucleotide Gated (CNG) channels. The recently determined crystal structure of a bacterial homolog of CNG channel pores, the NaK channel, revealed a Ca^{2+} binding site at the extracellular entrance to the selectivity filter. This site is not formed by the side chain carboxylate groups from the conserved acidic residue, Asp66 in NaK, conventionally thought to directly chelate Ca^{2+} in CNG channels, but rather by the backbone carbonyl groups of residue Gly67. Here we present a detailed structural analysis of the NaK channel with a focus on Ca^{2+} permeability and blockage using X-ray crystallographic methods. Our results confirm that the Asp66 residue, although not involved in direct chelation of Ca^{2+}, plays an essential role in Ca^{2+} binding at the extracellular entrance to the pore. Furthermore, we give evidence for the presence of a second Ca^{2+} binding site within the NaK selectivity filter where monovalent cations also bind, providing a structural basis for Ca^{2+} permeation through the NaK pore. Compared to other Ca^{2+}-binding proteins, both sites in NaK present a novel mode of Ca^{2+} chelation, using only backbone carbonyl oxygen atoms from residues in the selectivity filter. The

external site is under indirect control by an acidic residue (Asp66), making it Ca^{2+} specific. These findings give us a first glimpse at the molecular level of the possible underlying mechanisms allowing Ca^{2+} to act both as a permeating ion and blocker of CNG channels and raise the possibility of a similar chemistry governing Ca^{2+} chelation in Ca^{2+} channels.

Introduction

Cyclic Nucleotide gated (CNG) channels play an essential role in signal transduction pathways of, among others, visual and olfactory sensory systems [28-31]. Generally non specific for Group 1A monovalent cations, CNG channels also allow the passage of divalent cations like Ca^{2+} and Mg^{2+}, albeit at much slower rates, through their pores. This, in turn, leads to an effective blockage of monovalent currents [32-41]. Ca^{2+} blockage from the extracellular side, a property central to the physiological functioning of CNG channels [28], has been extensively studied using electrophysiological tools and is thought to arise primarily from the involvement of a conserved acidic residue, usually Glutamate, in the selectivity filter of the CNG channel [41-44]. Mutating this residue to a neutral amino acid has been shown to drastically decrease external Ca^{2+} blockage while substituting Glutamate with Aspartate preserved it. In the absence of structural information, it was previously speculated that the four conserved acidic residues of the channel tetramer, one from each subunit, point their side chains towards the ion

conduction pathway and directly chelate a Ca^{2+} ion with their carboxylate oxygen atoms.

The recently discovered NaK channel from *Bacillus cereus* provides a viable structural model for analyzing Ca^{2+} permeation in CNG channels. NaK has a selectivity filter sequence of $_{63}$TVGDG$_{67}$ similar to that of CNG channels (Fig. 2.7) and it also exhibits similar ion conduction properties: it conducts various monovalent cations [5] and monovalent cation conduction can be reduced by divalent cations (Fig. 2.8). A discrete Ca^{2+} binding site at the extracellular entrance to the pore was observed in the crystal structure of NaK, revealing a possible structural basis for external divalent cation blockage in CNG channels (Fig. 2.1). Contrary to expectations based on mutagenesis of CNG channels, the conserved acidic residue in the NaK filter (Asp66) does not directly bind Ca^{2+}. Instead, it is the four backbone carbonyl oxygen atoms of Gly67, one from each subunit, that chelate the Ca^{2+} ion. The side chain of Asp66 actually points away from the ion conduction pathway with its carboxylate group positioned at the opposite side of the Ca^{2+}-binding carbonyl group of Gly67 and very close to the amide nitrogen of the peptide bond between Gly67 and Gln68. Here we performed an extensive crystallographic study of the NaK channel and its mutants to analyze their Ca^{2+} permeability and blockage properties, with a particular focus on the role of Asp66 in specific Ca^{2+} binding at the extracellular entrance. Our

results reveal a novel mechanism underlying specific Ca^{2+} binding in NaK, which most likely applies to CNG channels also.

Results

Extracellular Ca^{2+} binding in D66E and D66N mutants. To test whether the conserved acidic residue (Asp66) in the NaK filter is important for Ca^{2+} binding, similar to what has been observed in CNG channels, mutant NaK channels were generated in which Asp66 was substituted with Glu (D66E) and Asn (D66N). Using ^{86}Rb flux assays, these mutants were shown to conduct monovalent cations like the wild type channel, indicating that the respective mutations did not affect the ion conduction properties of NaK (data not shown). Both the D66E and D66N mutants were crystallized in the presence of 200 mM $CaCl_2$ and their structures were determined at 2.6 Å and 2.4 Å, respectively (Methods and Table 1) and shown to be virtually identical to wild type. However, strong electron density of a bound Ca^{2+} ion at the external entrance of the filter was present in the D66E mutant, as in wild type, (Fig. 2A&B) but absent in the D66N structure (Fig. 2.2C&D), indicating a loss of external Ca^{2+} binding. The bound ion at the external entrance of the D66E filter was confirmed to be Ca^{2+} through soaking experiments which showed it is replaceable by Ba^{2+} but not monovalent cations (Rb^+ or Cs^+) (Fig. 2.9). Ca^{2+} binding at the external site therefore seems to be mediated primarily by the preservation of charge rather than side chain size. We also note that in contrast to wild type and D66E mutant channels, residues

forming the entrance to the pore region (residues 65-68) in the D66N mutant appear to have become more disordered (Fig. 2.2C), suggesting that Ca^{2+} binding to the entryway might rigidify the local structure.

Extracellular Ca^{2+} binding in D66AS70E and D66A. The D66E and D66N mutant structural data suggests that the presence of a negative charge in close proximity to the peptide bond between Gly67 and Asn68 is essential to mediate Ca^{2+} binding at the external site. To further test this hypothesis we designed a double mutant channel, D66AS70E, in which Asp66 was replaced by Ala and Ser70 was replaced by Glu. The double mutant structure was determined at 2.5 Å (Table 1) and revealed the carboxylate group from the original Asp66 residue replaced by one from Glu70 of a neighboring subunit (Fig. 2.3A). Consistent with our hypothesis, strong Ca^{2+} ion density was observed at the pore entrance in both $2F_o$-F_c and F_o-F_c ion omit maps (Fig. 2.3A&B). The presence of a bound Ca^{2+} ion at this site was further confirmed by soaking experiments performed with other monovalent (Rb^+ and Cs^+) and divalent (Ba^{2+}) cations (Fig. 2.10). As a control, the structure of an Asp66Ala (D66A) mutant channel was also determined at 2.3 Å (Table 1). Interestingly, Ca^{2+} binding was still observed in this structure (Fig. 2.3C&D) which, as discussed below, turned out to be much weaker than that observed in the wild type, D66E, and D66AS70E channels. A closer inspection of the D66A structure revealed an ordered water molecule in the exact location of the missing Asp66 carboxylate group (Fig. 2.3C). A partial negative charge on

this water molecule could weakly compensate for the missing negative charge contributed by Asp66 and, combined with the high concentration of Ca^{2+} in the crystallization conditions, likely accounts for the observed Ca^{2+} binding in the D66A mutant.

Relative Ca^{2+} binding affinities in wild type and mutant NaK channels.

For a comparison of relative Ca^{2+} binding affinities in the wild type and different mutant channels we soaked the respective protein crystals in stabilization solutions containing lower concentrations of Ca^{2+} (10 mM and 1 mM, see Methods). Figure 2.4A&B presents F_o-F_c ion omit maps generated from crystals subjected to these titration experiments. At 10 mM Ca^{2+}, density of externally bound Ca^{2+} was present in the wild type, D66E, and D66AS70E mutants but not observed in the D66A mutant (Fig. 2.4A). At 1 mM Ca^{2+}, Ca^{2+} density became weak in the wild type and D66AS70E mutant but remained strong in the D66E mutant, indicating higher Ca^{2+} binding affinity in D66E (Fig. 2.4B). The density of bound Ca^{2+} in D66E was shown to be abolished by soaking the crystals in a solution containing no Ca^{2+} (with 5mM EGTA, data not shown). A number of important conclusions can be drawn from this crystallographic titration assay. First, the loss of Ca^{2+} binding at 10mM Ca^{2+} concentration confirms that Ca^{2+} binding in the D66A mutant is very weak. Second, the results not only provide a qualitative picture of the relative Ca^{2+} affinities among wild type and mutant channels, which follows the following sequence: D66E > wild type ~ D66AS70E

> D66A > D66N, they also provide further support for the hypothesis that the presence of negative charge in the vicinity of Gly67 plays the determinant role in Ca^{2+} binding. Finally, the reduction and eventual loss of electron density at lower Ca^{2+} concentrations further confirms the specificity of the external site for divalent cations.

Second Ca^{2+} binding site within the NaK selectivity filter.

An interesting and physiologically significant property of CNG channels is their ability to conduct Ca^{2+} in addition to monovalent cations. Functional studies of Ca^{2+} permeation and blockage in CNG channels have pointed to the presence of multiple Ca^{2+} binding sites [34,42,45,46]. This prompted us to look for evidence of Ca^{2+} binding elsewhere in the NaK filter in addition to the external site. Site 3 in the NaK channel was previously shown by soaking experiments to bind Ba^{2+} in addition to monovalent cations[19], suggesting that Ca^{2+} might also bind here. A second indication of Ca^{2+}– binding at site 3 arose from a closer analysis of the Na^{+}- and K^{+}-complex structures of NaK (Table 2). The Na^{+} complex structure revealed much stronger electron density of bound ions at site 3 than at site 4 (Fig. 2.5A), whereas in the K^{+} complex structure electron density at both sites was roughly equivalent, that at site 4 being marginally stronger (Fig. 2.5B). Furthermore, we also determined the Rb^{+} complex structure of NaK at 2.6 Å which revealed noticeably stronger electron density at site 4 than at site 3 (Table 2 and Fig. 2.5C). Taking into account the number of electrons in these

various cations (Na^+=10e, K^+= Ca^{2+}=18e and Rb^+=36e) and the fact that monovalent cations bind at both sites 3 and 4 (based on previous soaking experiments), we predict the observed differences in relative intensity of the electron density at sites 3 and 4 could arise from Ca^{2+} (the only other cation present in crystallization conditions) binding at site 3 in addition to monovalent cations. To confirm this, we purified the NaK channel in LiCl, crystallized it in the presence of 200 mM $CaCl_2$, and determined its structure at 2.5 Å (Table 2). As shown in the F_o-F_c ion omit map, in addition to the external entrance of the pore, strong electron density was also observed at site 3 (Fig. 2.5D). Since the Li^+ ion has only two electrons, this strong density must come from a bound Ca^{2+} ion. Site 4 did not reveal any such density, indicating that Ca^{2+} binds preferably to site 3 within the NaK filter. Difference maps calculated from the Li^+-complex crystals soaked in a solution containing $BaCl_2$ gave rise to strong density at the external entrance and site 3, indicating that both Ca^{2+} ions can be replaced by Ba^{2+} (Fig. 2.5E). Although not a direct measurement of Ca^{2+} permeation in NaK, the structural observation that Ca^{2+} binds deep in the selectivity filter in addition to the external site raises the possibility of the NaK channel, like CNG channels, being permeable to Ca^{2+}.

Monitoring Ca^{2+} permeation in NaK using ^{45}Ca Flux assays.

NaK has so far proven to be averse to electrophysiological analysis, owing possibly to a low open probability and/or conductance. Additionally, the ^{86}Rb flux

assay employed for initial analysis of ion conduction in NaK is not sensitive enough to measure Ca^{2+} permeation in NaK, neither can this assay distinguish between internal and external blockage of NaK by Ca^{2+}. We therefore measured the uptake of Ca^{2+} directly in liposomes loaded with 400 mM KCl and reconstituted with NaKNΔ19, a truncated form of NaK lacking the N-terminal 19 residues, as support for our structural data. The method is similar to the ^{86}Rb flux assays except that ^{45}Ca is used as radioactive tracer (See methods). Results from these ^{45}Ca flux assays show time dependent accumulation of ^{45}Ca in liposomes containing NaK but not in control liposomes containing either no reconstituted protein or the K^+ conducting MthK pore [47], indicating that NaK likely conducts Ca^{2+} (Fig. 2.5F). The activity of the reconstituted proteins was also analyzed by ^{86}Rb flux assays, which showed strong, time dependent accumulation of ^{86}Rb in liposomes reconstituted with NaKNΔ19 or the MthK pore (data not shown), confirming that both had the ability to conduct K^+ and build up the required membrane potential for influx of ^{86}Rb or ^{45}Ca. These data, along with our structural studies, which were guided by functional and mutational analyses of Ca^{2+} permeation and blockage in CNG channels, offer a plausible structural basis for the so called 'permeating block' associated with Ca^{2+} permeability.

Discussion

Ca^{2+} binding motifs in most known Ca^{2+} binding proteins, although diverse, utilize oxygen atoms contributed by carboxylate, carbonyl, and hydroxyl groups, as well as water molecules as ligands [48,49]. Additionally, side chain carboxylate groups are always seen to act as ligands and most likely play a part in balancing the Ca^{2+} ion's positive charge. The mode of Ca^{2+} chelation in NaK, however, appears to be unique. The ion is chelated at both sites in the NaK pore exclusively by backbone carbonyl oxygen atoms rather than the carboxylate oxygen atoms of acidic residues. Only the external site is Ca^{2+} specific and our data suggest that this specificity arises from a through-space interaction between the Asp66 side chain and Gly67 backbone carbonyl group, most likely electrostatic in nature, which helps generate a highly favorable environment for Ca^{2+} chelation by the latter. A close up view of the region immediately surrounding residue 66 in NaK and its mutants (D66E, D66AS70E and D66A) provides a plausible explanation for the specificity of external Ca^{2+} binding in NaK that most likely applies to CNG channels also (Fig. 2.6A). A common feature among these NaK channels is the close proximity of the amide nitrogen atom of the Gly67/Asn68 peptide bond and the negatively charged oxygen atom from the side chain carboxylate group (Asp66 in wild type, Glu66 in D66E mutant, and Glu70 in D66AS70E) or partially charged oxygen atom from the water molecule in the D66A mutant. In our view, using the wild type channel as

an example, the most likely scenario places the negatively charged carboxylate oxygen atom of Asp66 close enough to the amide nitrogen of the Gly67/Asn68 peptide bond to stabilize its double bonded resonance form through a salt bridge like interaction (Fig. 2.6B). This, in turn, places a negative charge on the backbone carbonyl oxygen atom of Gly67 from each channel monomer, making it a more suitable ligand for Ca^{2+}. Our data also suggest that Ca^{2+} likely permeates the channel by subsequently binding to another intrapore binding site, site 3, which lacks the involvement of any acidic residues and is therefore non-specific and able to bind monovalent cations also.

The mechanism discussed above, whereby the properly positioned carboxylate group of Asp66, instead of binding Ca^{2+} directly, appears to confer Ca^{2+} specificity to the external Ca^{2+} binding site has intriguing implications for Ca^{2+} selectivity in Ca^{2+} channels, suggested to occur through similar mechanisms as those in CNG channels [29,31]. It is likely that Ca^{2+} channels also use backbone carbonyl groups to bind Ca^{2+} while the four acidic residues of the EEEE locus, shown by mutagenesis to be the sole element determining Ca^{2+} selectivity [50-52], confer Ca^{2+} specificity through similar mechanisms as seen here in NaK. This model is more readily reconciled with the plethora of evidence suggesting that Ca^{2+} channels have multi ion pores when compared to concurrent views of a single, flexible and rapidly rearranging Ca^{2+} binding site formed by the EEEE locus [24].

Materials and Methods

Protein preparation and crystallization. All genes encoding wild type and mutant NaK channel proteins were cloned into the pQE60 expression vector and expressed in *E.coli* XL1-Blue cells. NaK mutants were generated by Quick Change site directed mutagenesis (Strategene). Proteins were purified as tetramers in n-Decyl-β-D-Maltoside (DM) with NaCl, RbCl, or LiCl present as the monovalent salt. Crystals of wild type and mutant channels were grown using the sitting drop vapor diffusion method at 20 ^{o}C by mixing equal volumes of protein (30-35 mg/ml) and reservoir solution containing 200 mM $CaCl_2$, 100 mM Tris-HCl pH 8.0, 37-42 PEG400, and 4% t-Butanol. All crystals were of space group $C222_1$ with similar unit cell dimensions (Table 1 & 2).

Crystal soaking experiments. Mutant NaK crystals were soaked in stabilization solutions containing 40% PEG400, 100 mM Tris-HCl pH 8.0, 20 mM DM, 4% t-Butanol, 100 mM XCl, and 200 mM YCl_2, where X and Y represent a monovalent cation (Na^+, Rb^+ or Cs^+) and a divalent cation (Ca^{2+} or Ba^{2+}), respectively. To minimize nonisomorphism, data from the respective mutant crystals soaked in a stabilization solution containing 100 mM NaCl and 200 mM $CaCl_2$ was used as reference data against which all data from other soaked crystals were merged and scaled. For the titration analysis of Ca^{2+} affinity, the respective crystals were soaked in stabilization solutions containing 40% PEG

400, 100 mM Tris-HCl pH 8.0, 20 mM DM, 4% t-Butanol, 500 mM NaCl and 1 or 10 mM $CaCl_2$. The structures of those crystals used in the titration experiments were refined to resolutions between 2.8 Å and 3.1 Å.

Data collection and structure determination. All data were collected at the Advanced Photon Source (APS) and processed with HKL2000 [53]. Structures were determined by rigid-body refinement using the Na^+-complex structure of NaK as the initial model followed by iterative cycles of simulated annealing with torsion-angle dynamics in CNS [54] and model rebuilding in O [55]. Detailed statistics of data collection and refinement are listed in Table 1 and 2.

Protein Reconstitution and Flux Assays. The MthK pore and NaKNΔ19 constructs were purified as described previously[5,47]. The proteins were reconstituted in lipid vesicles composed of a 3:1 ratio of 1-palmitoyl-2-oleoyl-phosphatidylethanolamine and 1-palmitoyl-2-oleoyl-phosphatidylglycerol at a protein/lipid ratio of 6 and 10 μg/mg , respectively as described [56], with the following modifications: 10 mM DM was used to solubilize the lipid and dialysis (against a reconstitution buffer of 10 mM Hepes, pH 7.4, 400 mM KCl, and 4 mM NMG) was used to slowly remove the detergent from the detergent/lipid/protein mixture. The reconstituted liposome samples were kept at -80^{o}C in 100 ul aliquots.

^{86}Rb flux assays were performed as described previously [5,57] except that gel filtration through a pre-spun Sephadex G-50 fine resin soaked in 400 mM

Sorbitol, 4 mM NMG, and 10 mM Hepes pH 7.4 (Buffer A) was used to remove extraliposomal ^{86}Rb before measuring radioactivity levels in liposomes. ^{45}Ca flux assays were performed similarly to the ^{86}Rb flux assays except that ^{45}Ca was used as the radioactive tracer and buffer A was supplemented with 5mM $CaCl_2$.

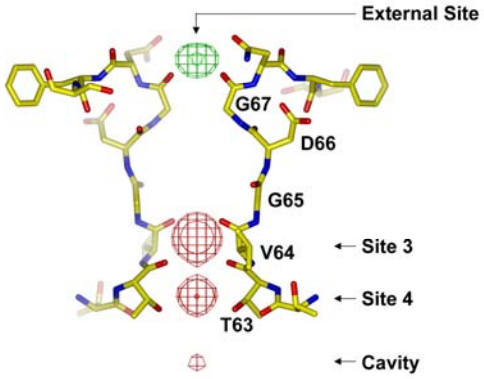

Figure 2.1 Structure of the NaK selectivity filter (accession number 2AHY) with F_o-F_c ion omit map contoured at 8 σ indicating the bound ions (green mesh for Ca^{2+} and red for Na^{+}).

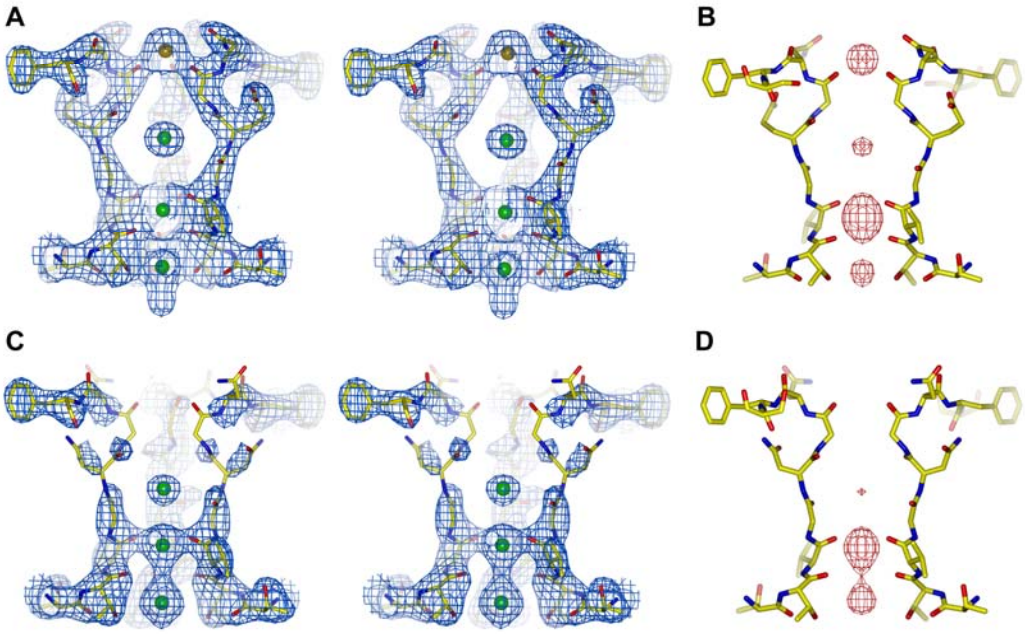

Figure 2.2 Structural analysis of NaK D66E and D66N mutants. (*A*) Stereo view of $2F_o$-F_c map (1.5 σ) of D66E at the filter region. The bound Ca^{2+} ion is modeled as an orange sphere. (*B*) F_o-F_c ion omit map (8 σ) at the D66E filter. (*C*) Stereo view of $2F_o$-F_c map (1.5 σ) of D66N at the filter region. (*D*) F_o-F_c ion omit map (8 σ) at the D66N filter.

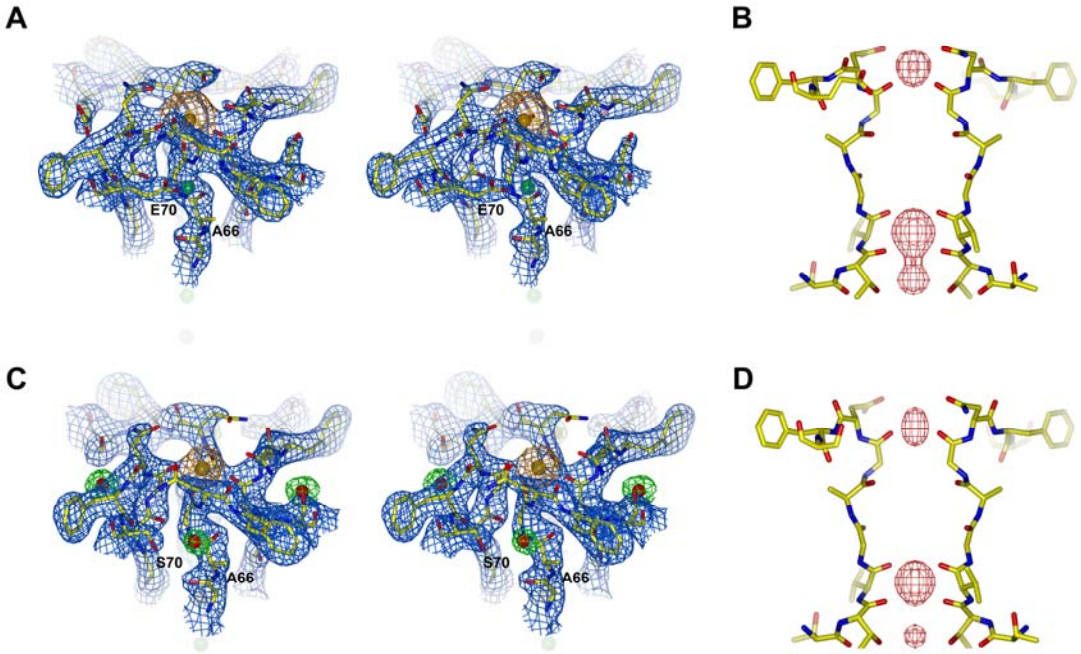

Figure 2.3. Structural analysis of NaK D66AS70E and D66A mutants. (*A*) $2F_o$-F_c map (1.5 σ) of the D66AS70E mutant around the external Ca^{2+} binding site. The density and sphere model of the Ca^{2+} ion are colored orange. (*B*) F_o-F_c ion omit map (8 σ) at the D66AS70E filter. (*C*) $2F_o$-F_c map (1.5 σ) of the D66A mutant around the Ca^{2+} binding site. The density and sphere model of the Ca^{2+} ion are colored orange. Density for water molecules (red spheres) is colored green. (*D*) F_o-F_c ion omit map (8 σ) at the D66A filter. Also refer to Fig. 6A for a zoom-in view of mutant NaK channels focused on the region surrounding residue 66.

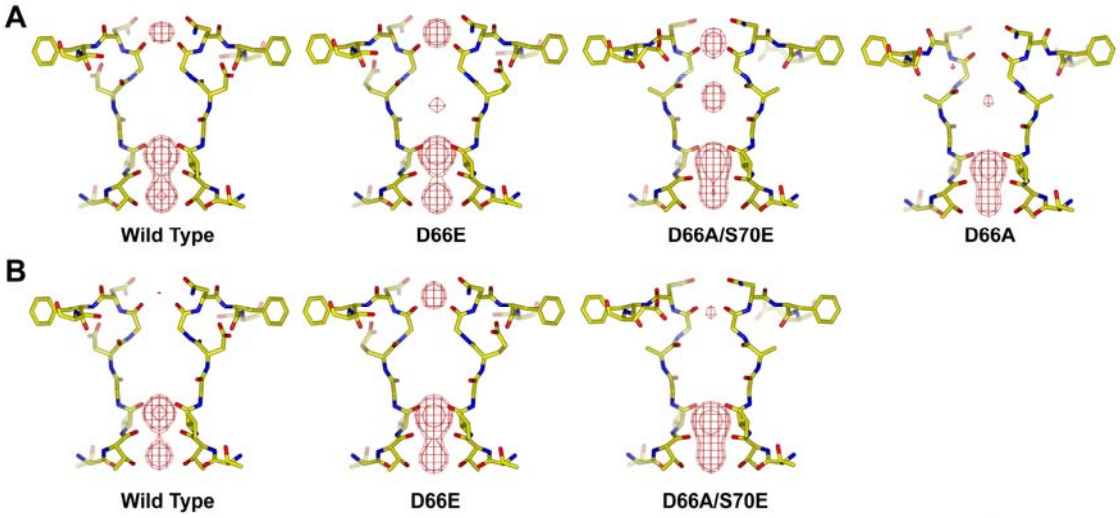

Figure 2.4. Titration analysis of Ca^{2+} affinity in NaK and its mutants**.** (*A*) and (*B*) are the F_o-F_c ion omit maps (6 σ) of wild type and mutant channel crystals soaked in stabilization solution containing 10 and 1 mM Ca^{2+} respectively

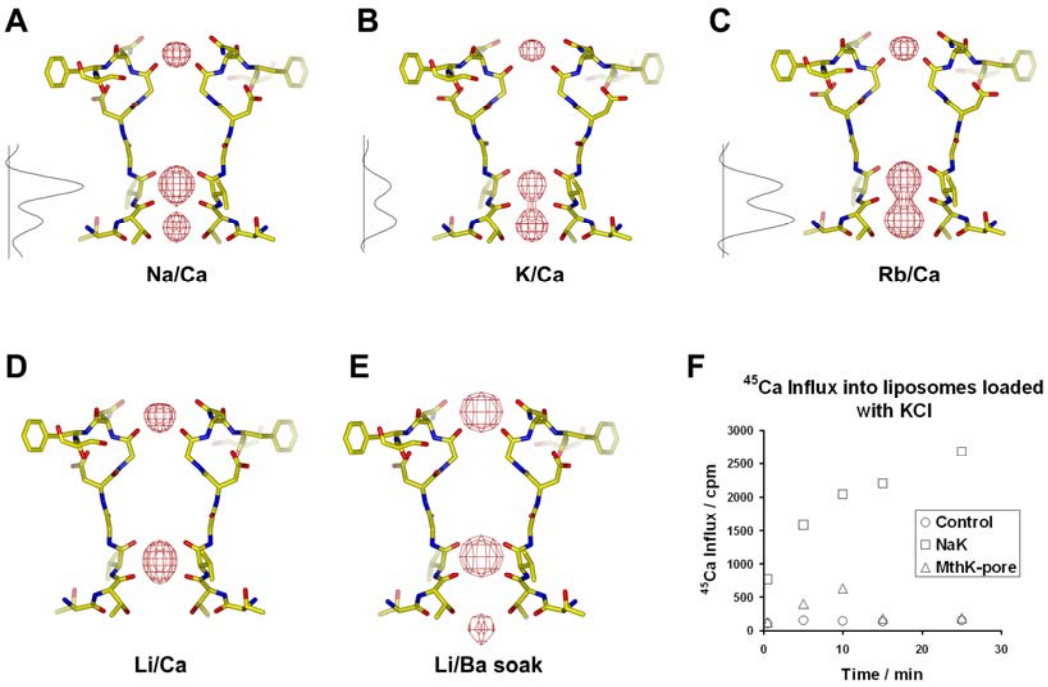

Figure 2.5. Structural study of NaK channels crystallized in the presence of different monovalent cations. All crystallization conditions contain 200 mM $CaCl_2$. Shown are F_o-F_c ion omit maps (8 σ) at the filter region calculated from crystals grown in the presence of 100 mM (*A*) NaCl (2.4 Å), (*B*) KCl (2.8 Å), (*C*) RbCl (2.6 Å) and (*D*) LiCl (2.5 Å). The maps of Na^+ and K^+ complexes were calculated from previously determined structures with accession numbers of 2AHY and 2AHZ, respectively. 1-D electron density profiles of bound ions at sites 3 and 4 in Na^+-, K^+- and Rb^+-complexes were obtained by sampling the F_o-F_c ion omit maps along the central axis of the filter. (*E*) 3.2 Å F_{soak}-$F_{reference}$ difference map (8σ) between crystal grown in LiCl/$CaCl_2$ (reference) and crystal soaked in LiCl/$BaCl_2$ (soak). (*F*) Time-dependent ^{45}Ca influx into liposomes loaded with 400 mM KCl and reconstituted with NaKNΔ19, MthK pore and no protein (as control).

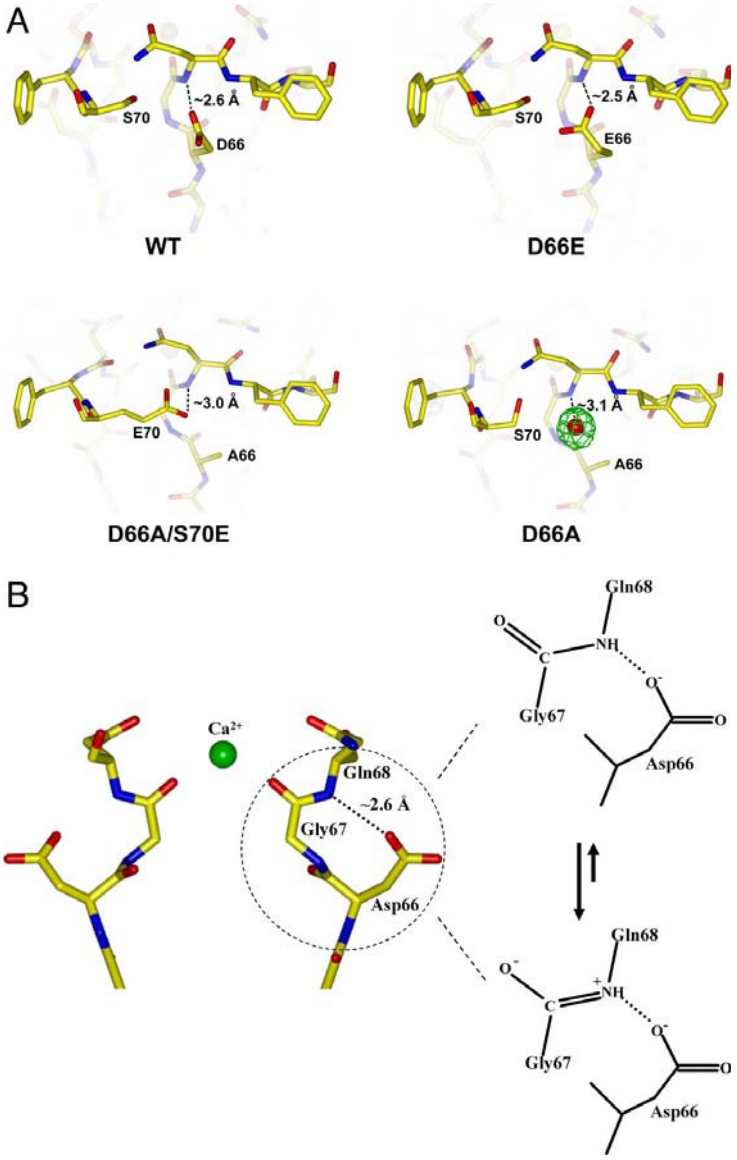

Figure 2.6 Mechanism for the specificity of external Ca^{2+} binding in NaK. (*A*) Zoom-in view of wild type and mutant NaK channels at the region surrounding residue 66. In wild type and D66E, the carboxylate oxygen atoms from D66 or E66 form Hydrogen bond interactions with the amide nitrogen of the Gly67/Asn68 peptide bond. In the D66A/S70E double mutant, the carboxylate oxygen of E70 from the neighboring subunit forms a similar hydrogen bond interaction with the same amide nitrogen. In D66A, a water molecule (red sphere with green mash representing its electron density) sits at the same position as the

carboxylate group in wild type channel and interacts with the amide nitrogen. Distances between the amide nitrogen of the Gly67/Asn68 peptide bond and the oxygen atoms involved in the hydrogen bond interaction are indicated. (*B*) Proposed mechanism underlying specific Ca^{2+} binding at the external entrance of the NaK filter mediated by the nearby acidic residue Asp66.

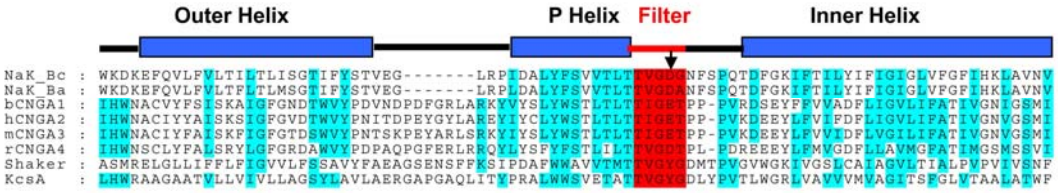

Figure 2.7 Sequence comparison of NaK with CNG and K^+ channels. Only pore regions have been included in the alignment with semiconserved residues and selectivity filters colored cyan and red, respectively. Arrow indicates the position of the conserved acidic residue in NaK (Asp-66) and CNG channels. Secondary structure assignment is based on the NaK crystal structure. The list of sequences includes NaK channels [*Bacillus cereus* (GI: 30018851) and *Bacillus anthracis*(GI: 47525956)]; CNG channels [bovine CNG α1 (GI:31342442), human CNG α2 (GI:42718010), mouse CNG α3 (GI:33859523), and rat CNG α4 (GI:16758252)]; and K^+ channels [*Shaker* from *Drosophila melanogaster* (GI: 288442) and KcsA from *Strptomyces lividans* (GI: 61226909)].

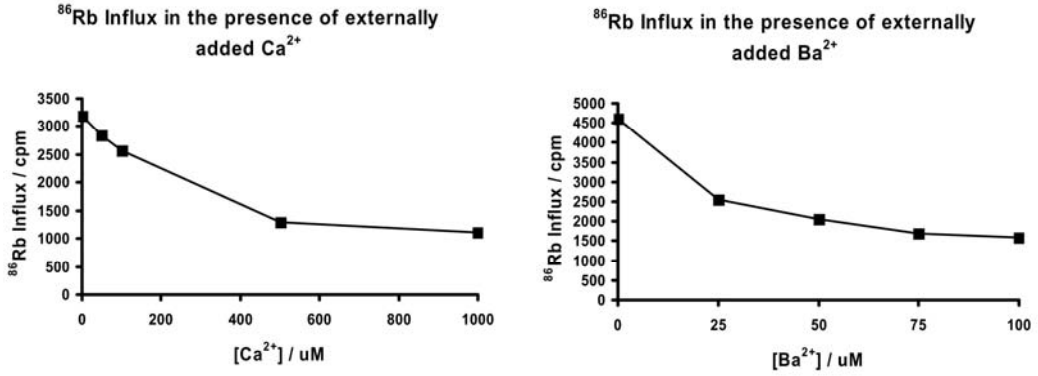

Fig. 2.8. ^{86}Rb influx in NaKNΔ19-containing liposomes in the presence of external Ca^{2+} (left panel) and Ba^{2+} (right panel) at different concentrations in addition to ^{86}Rb. The assay was performed as described previously (1). Liposomes were prepared in 400 mM NaCl. Flux was allowed to proceed for 20 min before radioactivity levels in liposomes were measured. Both divalent cations reduce ^{86}Rb influx in a concentration dependent manner, with Ba^{2+} having a much stronger effect than Ca^{2+}.

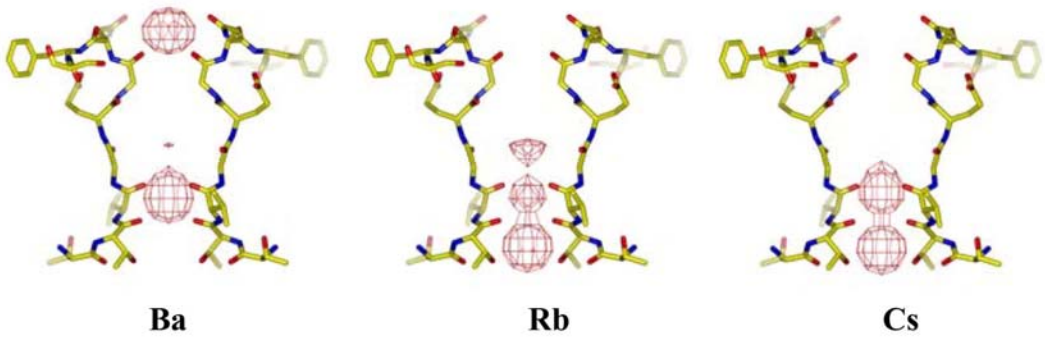

Figure. 2.9 To determine the ion binding profiles within the selectivity filters of the D66E mutant channel, mutant crystals were soaked in stabilization solutions containing 40% PEG400, 100 mM Tris-HCl, pH 8.0, 20 mM DM, 4% t-Butanol, 100 mM XCl, and 200 mM YCl_2, where X and Y represent a monovalent cation (Na^+, Rb^+ or Cs^+) and a divalent cation (Ca^{2+} or Ba^{2+}), respectively. To minimize nonisomorphism, data from a crystal soaked in a stabilization solution containing 100 mM NaCl and 200 mM $CaCl_2$ was used as reference data against which data from all other soaked crystals were merged and scaled. Shown are F_{soak} - $F_{reference}$ difference maps between the reference crystal and crystals soaked in stabilization solution containing Na/Ba(left panel), Rb/Ca (middle panel) or Cs/Ca (right panel). The results show that the bound ion at the external entrance of D66E filter can be replace by Ba^{2+} but not monovalent cations (Rb^+ or Cs^+), confirming it to be Ca^{2+}. All maps were calculated using data within a resolution range of 15-3.0 Å and contoured at 8 σ.

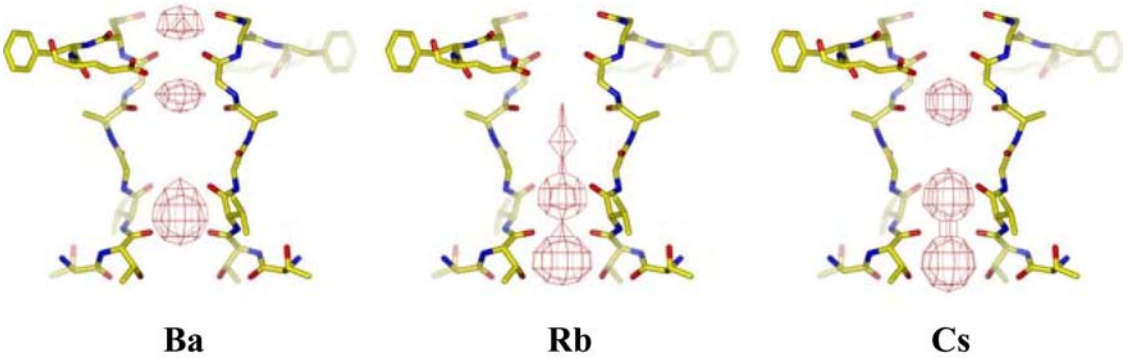

Fig. 2.10. Ion binding in the selectivity filter of the D66AS70E double mutant. The Same soaking experiments were performed as described in SI Fig. 9. Shown are F_{soak}-$F_{reference}$ difference maps between the reference crystal and crystals soaked in stabilization solution containing Na/Ba (*Left*), Rb/Ca (*Middle*) or Cs/Ca (*Right*). The results show that the bound ion at the external entrance of D66AS70E filter can be replaced by Ba^{2+} but not monovalent cations (Rb^{+} or Cs^{+}), confirming it to be Ca^{2+}. All maps were calculated using data within a resolution range of 15-3.2 Å and contoured at 8 σ.

Table 2.1. Data collection and refinement statistics for NaK mutants

	D66E	D66N	D66A/S70E	D66A
Data Collection[a]				
Space group	$C222_1$	$C222_1$	$C222_1$	$C222_1$
Cell dimensions				
a, b, c (Å)	82.0, 85.6, 130.1	82.3, 85.7, 130.6	82.3, 85.2, 130.2	82.2, 85.3, 130.2
Wavelength	0.9805	0.9793	0.9790	0.9786
Resolution range (Å)	50-2.6	50-2.4	50-2.5	50-2.3
R_{sym}	7.0 (91.9)	5.7 (98.2)	4.2 (59.4)	5.2 (82.9)
I/σ	20.0 (2.1)	27.7 (2.9)	35.1 (1.8)	39.0 (2.7)
Completeness (%)	97.1 (96.9)	99.5 (98.0)	96.1 (90.8)	94.5 (82.2)
Redundancy	5.4	7.4	5.1	5.3
No. reflections	14211	18352	15626	19529
Refinement				
Resolution range (Å)	50-2.6	50-2.4	50-2.5	50-2.3
R_{work}/ R_{free}[b] (%)	24.5 / 28.0	24.0 / 26.7	24.1 / 26.2	23.5/26.7
No. Atoms				
Protein / solvent / ion	1650 / 17 / 5	1648 / 34 / 3	1648 / 17 / 5	1642 / 40 / 3
R.m.s deviations[c]				
Bond lengths (Å) / angle(°)	0.006 / 1.20	0.007 / 0.97	0.007 / 1.09	0.006 / 1.06

[a] Numbers in parentheses are statistics for the highest resolution shell.
[b] 5 % of the data was used in the R_{free} calculation.
[c] R.m.s deviations = root-mean-square deviations

Table 2.2 Data collection and refinement statistics for NaK crystals grown in various monovalent cations

	NaK - Na[d]	NaK - K[d]	NaK - Rb	NaK - Li
Data Collection[a]				
Space group	$C222_1$	$C222_1$	$C222_1$	$C222_1$
Cell dimensions				
a, b, c (Å)	81.5, 85.5, 129.6	82.2, 85.5, 129.6	82.2, 85.8, 129.8	82.3, 85.6, 130.6
Wavelength	0.9795	1.5498	0.9795	0.9786
Resolution range (Å)	50-2.4	50-2.8	50-2.6	50-2.5
R_{sym}	4.5 (55.5)	5.1 (47.4)	4.2 (49.8)	6.1 (72.6)
I/σ	35.1 (1.8)	39.0 (2.7)	29.0 (1.2)	31.8 (2.0)
Completeness (%)	97.7 (84.1)	98.7 (94.3)	91.6 (51.2)	99.6 (100)
Redundancy	5.0	8.8	4.3	6.8
No. reflections	17659	11424	13519	16276
Refinement				
Resolution range (Å)	50-2.4	50-2.8	50-2.6	50-2.5
R_{work}/ R_{free}[b] (%)	23.5 / 26.0	24.1/28.0	23.6 / 25.6	23.4/25.8
No. Atoms				
Protein / solvent / ion	1648 / 20 / 5	1655 / 15 / 5	1648 / 24 / 4	1648 / 31 / 2
R.m.s deviations[c]				
Bond lengths (Å) / angle(º)	0.006 / 1.08	0.007 / 1.16	0.007 / 1.13	0.007 / 1.12

[a] Numbers in parentheses are statistics for the highest resolution shell.
[b] 5 % of the data was used in the R_{free} calculation.
[c] R.m.s deviations = root-mean-square deviations
[d] Previously determined structures with accession numbers 2AHY (Na) and 2AHZ (K).

CHAPTER THREE

High resolution structure of the open NaK channel.

We report the crystal structure of the non-selective cation channel NaK from *b. cereus* at a resolution of 1.6 Å. The structure reveals the intracellular gate in an open state compared to the closed form reported previously, making NaK the only channel for which the three-dimensional structures of both conformations are known. Channel opening follows a conserved mechanism of inner helix bending utilizing a flexible glycine residue, the gating hinge, seen in MthK and most other tetrameric cation channels. Additionally, distinct inter and intra-subunit rearrangements involved in channel gating are seen and characterized for the first time along with inner helix twisting motions. Furthermore, we identify a residue deeper within the cavity of the channel pore, Phe92, which likely forms a constriction point within the open pore, restricting ion flux through the channel. Mutating this residue to Ala causes a subsequent increase in ion conduction rates as measured by ^{86}Rb flux assays. The structures of both the open and closed conformations of the NaK channel correlate very well with those of equivalent K^+ channel conformations, namely MthK and KcsA, respectively.

The opening and closing of ion channel pores in response to external stimuli such as voltage or ligand binding is a process of extreme importance to ion channel physiology[1]. Up till now, our knowledge of the open and closed conformations of tetrameric cation channel pores comes predominantly from the crystal structures of various K^+ channels, among which the structures of KcsA and MthK have been generally accepted as reasonable models for the closed and open conformations of tetrameric cation channel pores, respectively [2,6,8,12-15,58]. The closed conformation is characterized by near straight inner helices and the subsequent bundle crossing formed by interactions between their c-terminal residues. In the open conformation seen in the MthK structure, the inner helices appear to bend at a conserved glycine residue, the gating hinge also seen in most other cation channels, resulting in the disruption of the bundle crossing. However, structural information on both states from the same channel has so far been lacking.

In the process of studying the ion selectivity properties of the NaK channel which shares overall sequence and structural similarities with KcsA except in the selectivity filter region and conducts both Na^+ and K^+ [3,5], we crystallized a truncated construct (NaKNΔ19) lacking its N-terminal M0 helix and determined its structure at a resolution of 1.6 Å. To our surprise, the NaKNΔ19 structure reveals the intracellular gate in an open conformation. Combined with the closed conformation structure of NaK, the new structure provides a unique opportunity

to analyze in detail the structural features underlying pore opening and closing within the same channel. We observe both inner helix twisting and bending at the glycine gating hinge upon pore opening. Our data clearly demonstrate the conservation of central sequence and structural motifs involved in channel opening, while also offering insight into the intricate rearrangements of interactions within and between channel subunits upon undergoing gating transitions. In addition, the high resolution structures also allow us to carry out an analysis of the molecular details of ion binding in the NaK selectivity filter, which we report in chapter 4.

Overall structure of the open NaK channel

NaKNΔ19 was crystallized in the presence of various monovalent cations (NaCl, KCl, or RbCl) (Methods). Numerous structures of NaKNΔ19 in different salts were determined by molecular replacement and refined to resolutions between 1.6 Å and 2.0 Å. Only the 1.6 Å structure is discussed here whereas all other structures are discussed in the companion paper focusing on ion selectivity. All crystals were of space group I4 and contained two subunits per asymmetric unit. Interestingly, each subunit uses three crystallographic 4-fold related counterparts to form a functional channel tetramer. In other words, the molecular 4-fold coincides with the crystallographic tetrad and the crystal contains two sets of channel tetramers with virtually identical structures except for minor differences in B-factor distribution.

In comparison to NaK, the NaKNΔ19 structure apparently adopts an open conformation at its intracellular gate (Fig. 3.1a). Superimposition of the structures of NaKNΔ19 and NaK with its M0 helix removed, viewed along the plane of the membrane with proximal and distal subunits removed (Fig. 3.1b) and from the intracellular side (Fig. 3.1c), reveal conformational changes of the NaK intracellular gate upon opening and closing. The regions surrounding the selectivity filter in both structures (residues 35 to 85) are almost identical with a main chain root-mean-square deviation (RMSD) of 0.35Å, which suggests that this region remains static during channel gating. Major structural changes appear to occur in the pore lining inner helices just below the selectivity filter. The inner helices in the NaK structure appear to be nearly straight, reminiscent of the KcsA structure, whereas those in NaKNΔ19 appear to develop a bend (about 34°, Fig. 3.1d) that splays the intracellular gate wide open as seen for the MthK open pore structure[15]. This inner helix bending occurs at residue Gly87 in NaK, shown by sequence alignment (Fig. 3.4) to be the conserved gating hinge glycine seen in MthK and other selective and non-selective cation channels. In addition to a simple bending motion, the inner helices also undergo a 45º clockwise twist around their helical axis as viewed from intracellular side (Fig. 3.1d). Along with inner helix bending, the outer helices tilt tangentially in the same direction by about 11º without any twisting motion (Fig. 3.1c).

Structural conservation in the open and closed NaK channel pores.

Despite the structural difference between the selectivity filters of NaK and K^+ channels, their overall tertiary structures, comprising the inner and outer helices along with the pore helix, are virtually identical. The availability of both closed and open conformation structures of the NaK channel at high resolution allows us to compare and analyze the global arrangement of these three structural elements in NaK with those in K^+ channels structures of equivalent pore conformations. Figure 3.1e shows such a comparison of the closed and open structures of NaK with KcsA and MthK, respectively. In the closed conformation, the inner and pore helices of NaK superimpose very well with those of KcsA with a main chain RMSD of 0.73 Å, whereas the respective outer helices are slightly shifted translationally (Fig. 3.1e, left). In the open conformation, all three components of NaKNΔ19 and MthK (outer, inner, and pore helices) superimpose very well with a main chain RMSD of 0.74 Å (Fig. 3.1e, right). Considering the fact that these four structures are from three different channels crystallized in different conditions, the observed structural and positional conservation of the pore-lining inner helices is a clear indication of conserved gating mechanics in tetrameric cation channels. Since the major conformational changes upon channel gating occur within the inner helices in both NaK and K^+ channels, the position of outer helices does not seem to require the same level of conservation as their pore lining counterparts. This was also seen in a structural

comparison of the KcsA and Kir channels where their respective outer helices did not superimpose well compared to the inner helices [58].

Inter/intra subunit interactions in the closed and open NaK channel.

The determination of high resolution structures for both the open and closed conformation of the NaK channel allows us, for the first time, to visualize the rearrangement of intra and inter-subunit protein contacts within the same channel pore upon gating. The intra-subunit interaction between inner and outer helices remains similar between closed (Fig. 3.2a, zoom 1) and open (Fig. 3.2b, zoom 1) conformations as a consequence of the concurrent movement of both helices and inner helix twisting. However, the inter-subunit interactions between neighboring inner helices at the bundle crossing seen in the closed NaK structure (Fig. 3.2a, zoom 3) are disrupted upon pore opening. It is also interesting to note that a major change in inter-subunit interaction occurs at the region just above the bundle crossing. In the closed conformation, Phe92 from each inner helix forms contacts with a hydrophobic patch on the opposite face of Phe92 from the neighboring inner helix formed by Val91, Phe94, Ile95 and Leu98 (Fig. 3.2a zoom 2). Inner helix bending in the open conformation causes Phe92 to swing away and point its side chain towards the central ion conduction pathway. However, the hydrophobic patch also slides along the neighboring inner helix by two helical turns and forms new van der Waals contacts with Phe85 (Fig. 3.2b, zoom 2).

Effect of ion conduction pathway size on channel conduction

In the closed NaK channel, side chains from residues Ile95, Ala99 and Gln103 at or above the bundle crossing form several constriction points along the ion conduction pathway, with the intracellular gate almost completely sealed off by the side chain of Gln103 (Fig. 3.2a, zoom 3). The bending of inner helices upon channel opening disrupts this bundle crossing. However, a new constriction point is created by the side chain of residue Phe92 (Fig. 3.1a and Fig. 3.3a). It is interesting to note that residue positions equivalent to Phe92 in NaK are occupied by small side chain amino acids in most other cation channels, most notably alanine as in MthK where it forms the narrowest part of the open pore [15](Fig. 3.4). By roughly orienting its aromatic ring towards the central ion conduction pathway, Phe92 forms a constriction point in the open NaK pore with an ion pathway diameter of about 6.5 Å (Fig. 3.3a), which is narrower than what is seen in the open MthK channel (~ 9.5 Å) and is likely to lower ion conduction rates. Indeed, the structure of a Phe92Ala mutation shows an ion conduction pathway comparatively less hindered by steric barriers (Fig. 3.3b) with a diameter of 10.5 Å at the constriction point and expectedly leads to increased accumulation of Rb^{86} in liposomes (Fig. 3.3c). Although the effects of this mutation on increasing channel open probability in NaK cannot be discounted based on results from the ^{86}Rb flux assay, our recent electrophysiological study on equivalent mutations in

MthK shows an obvious change in ion conduction rates (Y. Li, S. Ye, and Y.J, unpublished data). This supports the suggestion that a small side chain residue at this position is important in allowing for a wider ion passageway and easier access to the selectivity filter in cation channels as previously proposed[15].

Discussion

In this study we present a high resolution structure of the NaKNΔ19 channel in an open conformation. A comparison of this open state structure with that of the previously determined closed state shows that the region surrounding the selectivity filter, the top 1/3 of the pore at towards the extracellular side, remains static during channel gating. In contrast, major conformational changes occur in the inner helices at residue Gly87 just below the filter. The structure similarity between NaKNΔ19 and MthK pore points to similar pore opening mechanics in these two channels, specifically, utilization of a conserved glycine residue as a gating hinge to allow for inner helix bending. This glycine hinge has also been functionally shown to be important for gating in other tetrameric cation channels, such as voltage-gated K^+ and Na^+ channels [59-62], although these channel pores may not open as wide as what is observed in MthK or NaK.

Even though the intra- and inter-subunit interactions in the open state of NaK appear to be less extensive than those in the closed state, mainly due to the disruption of the helix bundle crossing, a number of factors could contribute to the stabilization of the open state captured in the crystal. First, the M0 helices are

absent in NaKNΔ19. In the closed NaK structure, four M0 helices form a cuff surrounding the bundle crossing and could prevent the inner helices from splaying open, a spatial hindrance absent in the truncated construct. Indeed, NaKNΔ19 does functionally display substantially higher ion conduction rates compared to the full length channel in ^{86}Rb flux assays[5], which most likely stems from a higher channel open probability. Second, the use of detergents instead of lipids in the purification and crystallization procedures, in other words the absence of a lipid environment in the crystal, could allow for more conformational freedom for the channel. Finally, protein packing in the crystal could be a main factor contributing to the open state. Two kinds of inter-tetramer packing interactions were observed in the NaKNΔ19 crystal (Fig. 3.5). One is the anti-parallel hydrophobic packing between outer helices from two neighboring channel tetramers (Fig. 3.5, squared region). The other is hydrophilic contacts between the C-terminal end of the inner helix and the extracellular surface of a neighboring tetramer (Fig 3.5, circled regions). These hydrophilic contacts are predominantly hydrogen bonding in nature and some are mediated by water molecules. Since both kinds of inter-tetramer packing interactions are quite extensive, we believe this is the dominant force stabilizing NaKNΔ19 in the open conformation. Despite the possibility of structural distortion due to crystal packing, the fact that NaKNΔ19 and MthK, two different crystals of different proteins, share virtually the same structure is a clear indication that NaKNΔ19 does represent an open pore structure.

KcsA has been one of the most well studied K^+ channels in regards to its gating properties, specifically the physical movement of its intracellular gate [63-71]. The global conformational changes observed between the open and closed conformation structures of NaK match quite well with those observed in KcsA. In a recent study using single KcsA tetramers labeled with gold nano crystals, a global twisting motion of +/- 40º was observed for inner helices in channels undergoing gating transitions[71]. Such a movement can be easily mapped on to the NaK structures. By using the Cα of Ala99 as an example, the movement of residues at the C-terminal part of inner helices between closed and open state results in a rotation of about 42º relative to the central axis (Fig. 3.6), equivalent to the global twisting motion reported for the KcsA pore.

It is also important to note that some of the cross subunit (diagonal) distances calculated between residues in the open and closed conformation of NaK are quite different from those reported in a gating study on KcsA using Electron Paramagnetic Resonance (EPR) spectroscopic methods [64,65]. For example, the distance between two spin-labeled Ala109s in KcsA shows a decrease of about 9 Å from closed to open states in the EPR measurement, whereas the diagonal distance between the Cβs of the equivalent residues (Lys97) in NaK show an increase of 5.5 Å from closed to open state based on our crystal structures. We believe this discrepancy arises mainly from contributions of the

spin label arm length, which can extend up to 9 Å from the Cβ of the labeled residue and the paramagnetic center in the nitroxide moiety [72], rather than from differences in gating mechanics. As shown in Fig 3.6b, in the closed state of NaK, Lys97 is positioned at the distal face of the inner helix relative to the central axis of the pore. A spin label at this position likely has the nitroxide moiety extended away from the central axis leading to an overestimation of the diagonal distance. On the other hand, Lys97 in the open state would be oriented more towards the ion conduction pathway as a consequence of inner helix bending and twisting and the spin label at this position will have the nitroxide moiety extending closer to the central axis leading to an underestimation of the diagonal distance. If we measure the diagonal distance between the amine atoms of Lys97s instead of Cßs as a simple approximation of the distance between the paramagnetic centers, a decrease of 7 Å is observed (from 29 Å in the closed state to 22 Å in the open state), which matches well with that observed in the EPR measurement of KcsA labeled at the equivalent residue (Ala109). Here we only consider one residue as an example instead of mapping and comparing every relevant NaK residue with corresponding KcsA residues in the EPR studies. The important conclusion that arises, however, is that the structure of KcsA in its open state would likely be similar to that of NaKNΔ19 or MthK and the structures of NaK and NaKNΔ19 represent the general structures of the tetrameric cation channel pore in closed and open states, respectively.

Methods

Protein expression and purification. We cloned the gene encoding the NaKNΔ19 channel, a truncated form of the NaK channel lacking the N-terminal 19 residues, into the PQE60 expression vector between *NcoI* and *BamHI* restriction endonuclease sites with a thrombin cleavage site between a C-terminal hexahistidine sequence and the channel. The Phe92 to Ala mutant was generated using the Strategene Quick Change II site directed mutagenesis kit. The channels were expressed in *E. coli* XL1 Blue or SG13009 cells by induction (at A_{600} ~ 0.8) with 0.4 mM isopropyl-β-D-thiogalactopyranoside (IPTG) at 25ºC for 20 hours. Cells were harvested and lysed in a solution of 50 mM Tris·HCl, pH 8.0, and 100 mM NaCl. Expressed protein was then extracted from the cell lysate for 3 hours at room temperature in the above solution by adding 40 mM n-decyl-β-D-maltoside (DM) and purified on a Talon Co^{2+} affinity column (Clontech). The column was first washed with 20 mM Tris·HCl, pH 8.0, 100 mM NaCl and 5 mM DM, then with the above buffer containing 15 mM imidazole to remove non-specifically bound proteins. Finally, the NaKNΔ19 channel was eluted with 300 mM imidazole. After elution, the protein was incubated overnight at room temperature (~ 20 °C) in the presence of 1 unit of thrombin per 2 mg of protein to remove the hexahistidine tag, and then further purified on a Superdex-200 (10/30) column in a solution of 20 mM Tris·HCl, pH 8.0, 100 mM NaCl and 5 mM DM.

Crystallization and structure determination

Purified proteins were concentrated to 12-20 mg ml^{-1} using an Amicon Ultra centrifugal filtration device (50kD MW cutoff) and crystallized using the sitting drop vapor diffusion method by mixing equal volumes of concentrated protein and well solution. The highest resolution (1.6Å) structure used in this discussion was determined from crystal grown over a well solution containing 55-70% (v/v) (±)-2-Methyl-2,4-pentanediol (MPD), 1 mM $CaCl_2$ and 100 mM Glycine pH 9.5. All crystals were frozen in liquid propane with the crystallization solution serving as the cryo-protectant. Crystals were of space group I4 with unit cell dimensions around $a=b=68$ Å, $c = 89$ Å, $\alpha=\beta=\gamma=90^{o}$ and contained 2 molecules per asymmetric unit. The four-fold axis of the channel tetramer coincided with the crystallographic tetrad.

X-ray data were collected at the Advanced Photon Source (APS) Beamlines 19-ID/BM and 23-ID. Data processing and scaling was performed using the HKL2000 software [53]. The structures were determined by molecular replacement using Molrep in the CCP4 suite [73] using the region surrounding the filter of the full length NaK structure (residues 30 to 90, PDB code 2AHY) as an initial search model followed by repeated cycles of model building in O [55] and refinement in CNS [54]. 95.1 % of the residues were in most favored regions and 4.9 % in additionally allowed regions on a Ramachandran plot. Some discontinuous

electron density can be attributed to bound lipid, detergent, or other solvent molecules and was assigned as water molecules for simplicity. Detailed data collection and refinement statistics are listed in Table I.

All structure figures were generated in Pymol (www.pymol.org) with the exception of the surface renderings of the ion conduction pathways of NaKNΔ19 and its F92A mutant, which were calculated in the program HOLE [74] and rendered in VMD [75].

^{86}Rb flux assay

All channel proteins used in the flux assay were purified in the detergent DM and reconstituted into lipid vesicles composed of 1-palmitoyl-2-oleoyl-phosphatidylethanolamine (POPE, 7.5 mg ml^{-1}) and 1-palmitoyl-2-oleoyl-phosphatidylglycerol (POPG, 2.5 mg ml^{-1}) at a protein/lipid ratio of 5-10 μg mg^{-1} using the same method as described[56,5756,5749,5056,5749,5042,43][32, 33] with the following modifications: 10 mM DM was used to solubilize the lipid and dialysis (against a reconstitution buffer of 10 mM Hepes, pH 7.4, 400 mM NaCl or KCl, and 4 mM NMG) was used to slowly remove the detergent from the detergent/lipid/protein mixture. The reconstituted liposome samples were kept at -80^{o}C in 100 ul aliquots.

The ^{86}Rb flux assay was performed following virtually the same procedures as described[57]. Liposomes were thawed and sonicated in a bath

sonicator for 30 seconds before the assay. To remove extra-liposomal salt (NaCl or KCl), 95 ul samples were passed through a pre-spun Sephadex G-50 fine gel filtration column (1.5 ml bed volume in a 5 ml disposable spin column) swollen in 400 mM Sorbitol, 10 mM Hepes, pH 7.4 and 4 mM NMG. 160 ul of liposome samples collected after this buffer exchange step were added to 320 ul ^{86}Rb flux buffer (400 mM Sorbitol, 10 mM Hepes, pH 7.4, 4 mM NMG, 50 uM NaCl or KCl, and 5 uM ^{86}RbCl). 75ul of this reaction mixture were passed through another pre-spun gel filtration column as described above to eliminate extraliposomal ^{86}Rb at the desired time points. For normalization, 1ug ml^{-1} (final) valinomycin was added to the mixture for an additional 2 minutes before taking the final reading after the last gel filtration step. The final eluate was mixed with 10 ml scintillation cocktail and its radioactivity measured in a scintillation counter.

Coordinates. Protein Data Bank: The atomic coordinates and structure factors of NaKNΔ19 have been deposited (accession number 3E86).

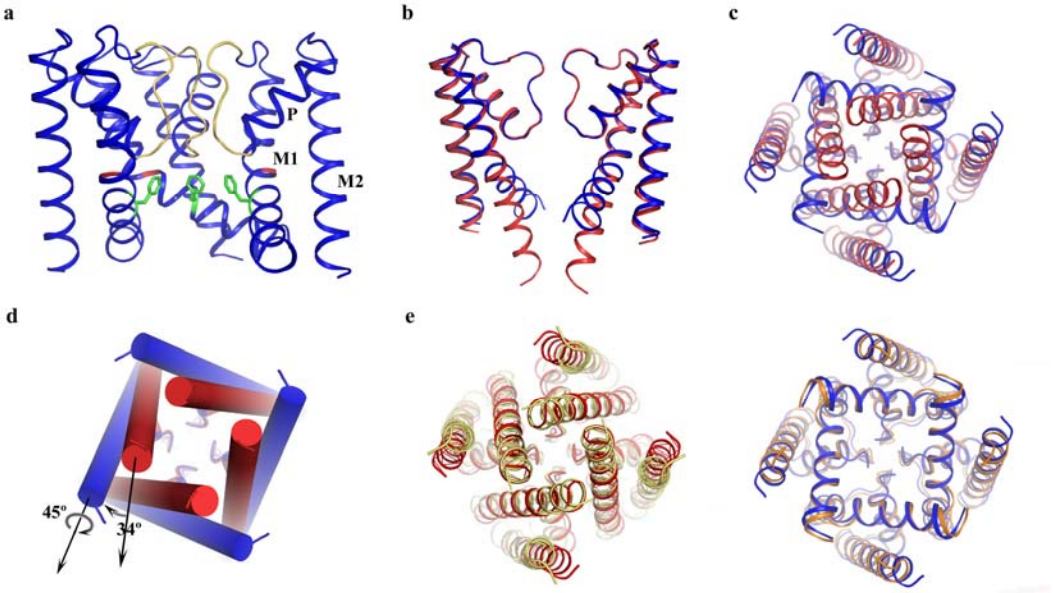

Figure 3.1 Structure of NaKNΔ19 in an open conformation. (**a**) Overall structure of NaKNΔ19 with the front subunit removed for clarity. Selectivity filter residues, Gly87 and Phe92 are colored yellow, red and green, respectively. M1=outer helix, M2=inner helix, and P=pore helix **b)** Superimposition of the structures of NaKNΔ19 (blue) and NaK (red, PDB code 2AHY) with its M0 helix removed, viewed from the plane of the membrane with proximal and distal subunits removed and **c)** from the intracellular side. **d)** Conformational change of NaK inner helices from the closed (red cylinder) to open state (blue cylinder) involves a 34º bending and a 45º twisting around the helical axis. **e)** Comparison of NaK with KcsA (left) and MthK (right). Superimposition of the closed NaK structure (red, PDB code 2AHY) with KcsA (yellow, PDB code 1K4C) viewed from the intracellular side along 4-fold axis and the equivalent superimposition of the open NaKNΔ19 structure (blue) with the MthK pore (orange, PDB code1LNQ) are shown.

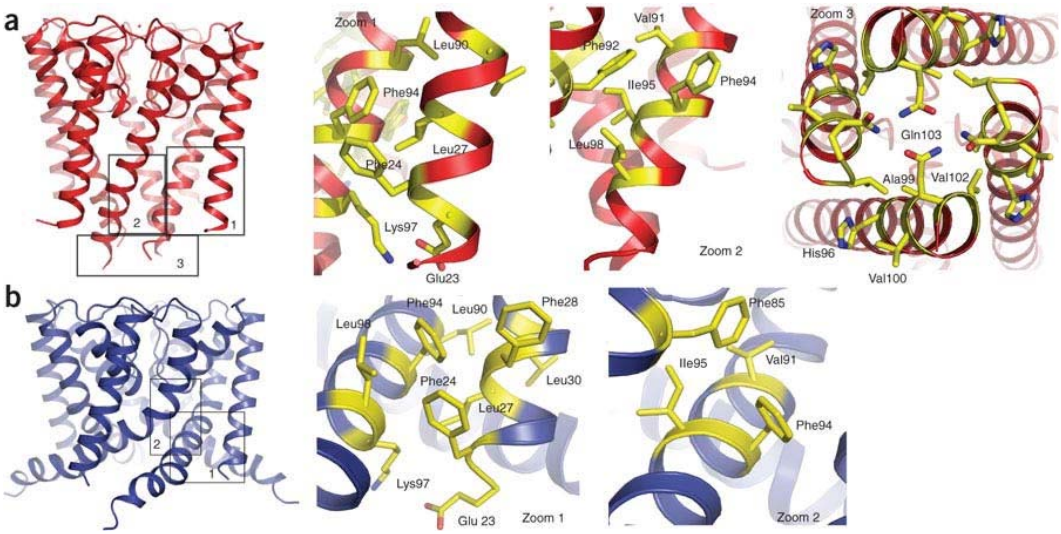

Figure 3.2 Analysis of inter and intrasubunit interactions in the closed (a) and open (b) structures of the NaK channel. The numbers in the boxed regions in both structures correspond to the zoomed in views 1–3 for the closed structure and 1 and 2 for the open NaK structure. Zoom 1 in both cases highlights intrasubunit interactions between outer (M1) and inner (M2) helices. Zoom 2 highlights intersubunit interactions between inner helices of two neighboring subunits. Zoom 3 shows an intracellular view of the interactions involved in the bundle crossing formation in the closed structure.

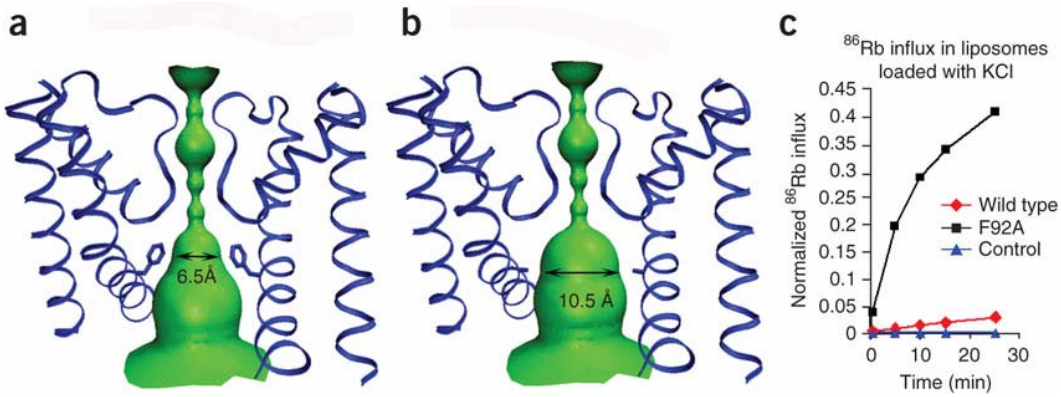

Figure 3.3 Effect of the size of the ion-conduction pathway on ion conduction in NaK.(a,b) Surface representation of the ion-conduction pathway of the NaKN⍙19 open pore (a) and its F92A mutant (b). (c) ^{86}Rb flux assay showing time-dependent Rb^{+} influx in liposomes reconstituted with NaKN⍙19 (red trace) and the F92A mutant (black trace). Both proteins were reconstituted in liposomes loaded with KCl at the same concentration. Liposomes with no reconstituted protein were used as a control (blue trace).

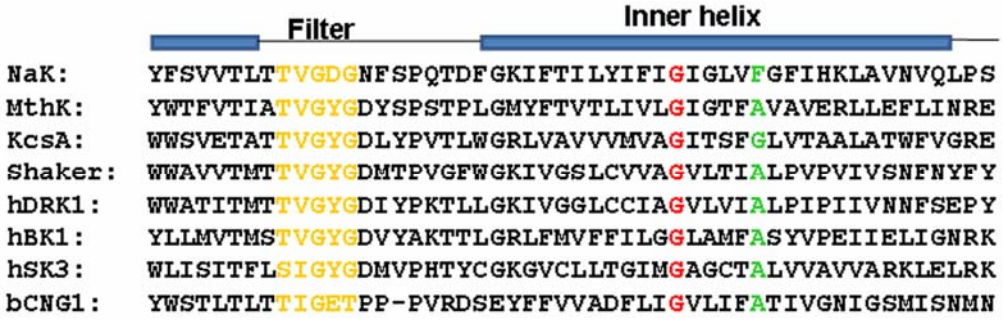

Figure 3.4. Partial sequence alignment of part of the NaK with those of various other tetrameric cation channels. Arrows indicate the conserved gating hinge glycine (red) and residue 5 amino-acids C-terminal to it (green), with residues forming the selectivity filter colored yellow.

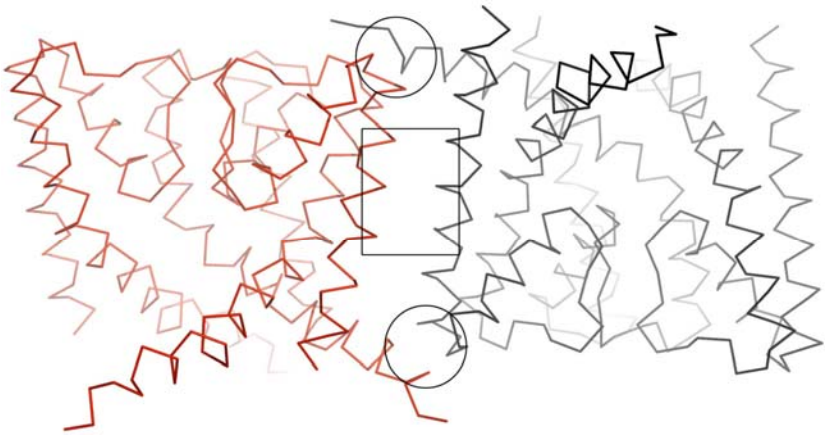

Figure 3.5 Packing interactions between two neighboring tetramers in the NaKNΔ19 crystal. Boxed and circled regions highlight the regions where the main interactions occur.

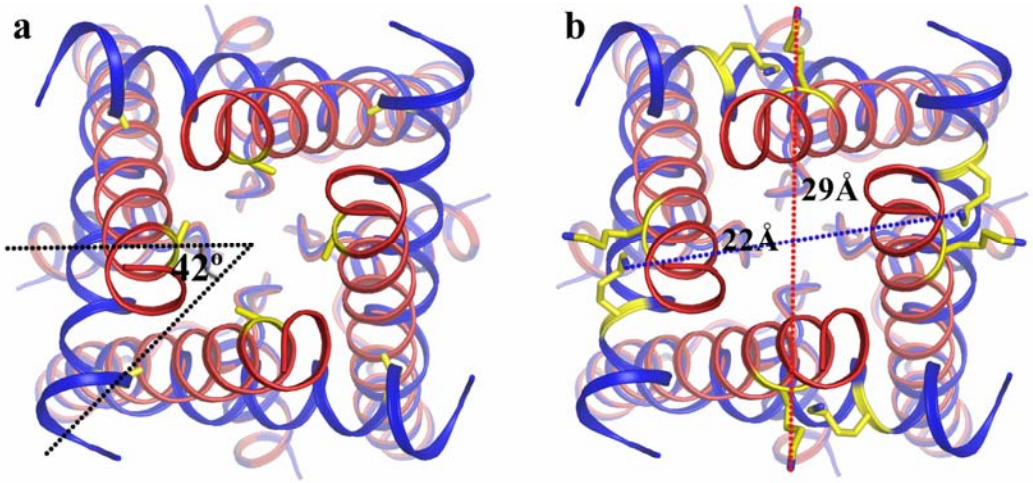

Figure 3.6 Mapping the global conformational changes of KcsA gating onto the NaK channel. Shown is the intracellular view of the NaK inner helices in the open channel (red ribbon) superimposed on those of the closed channel (blue ribbon). **a)** Mapping the global twisting motion of KcsA onto NaK. The angle indicates the angular movement of the Cα of Ala99 (yellow) relative to the central axis between closed and open states. **b)** Positions of Lys97s in closed and open NaK. Dotted lines indicate the diagonal distances between the amine atoms of Lys97s in closed (blue, 29 Å) and open (red, 22 Å) states.

Table 3.1 Data collection and refinement statistics (molecular replacement)

	NaKNΔ19 100mM Na^+ /1mM Ca^{2+}
Data collection	
Space group	
Cell dimensions	
a, *b*, *c* (Å)	68.030, 68.030, 89.264
α, β, γ (°)	90, 90, 90
Resolution (Å)	50-1.6
R_{sym} or R_{merge}	4.2 (48.4)
$I / \sigma I$	48 (1.5)
Completeness (%)	94.9 (62.4)
Redundancy	6.7(2.3)
Refinement	
Resolution (Å)	50-1.6
No. reflections	25448
R_{work} / R_{free}	
No. atoms	
Protein	1462
Ligand/ion	23
Water	152
B-factors	
Protein	35.629
Ligand/ion	42.35
Water	55.228
R.m.s. deviations	
Bond lengths (Å)	0.0090
Bond angles (°)	1.299

CHAPTER FOUR

Structural Analysis of Ion Selectivity in the NaK Channel

Here, we present a detailed characterization of ion binding in the NaK pore using the high resolution structures of NaK in complex with various cations. These structures reveal four ion binding sites with similar chemical environments but vastly different ion preference. The most non selective of all is site 3, which is formed exclusively by backbone carbonyl oxygen atoms and resides deep within the selectivity filter. Additionally, four water molecules are seen to form half hydration shells around K^+ and Rb^+ ions both at the external entrance and vestibule of the NaK filter, confirming the preference for an octahedral ligand configuration for K^+ and Rb^+ chelation. In contrast, Na^+ binding in the NaK filter, particularly at site 4, utilizes a pyramidal ligand configuration requiring the participation of a water molecule in the cavity. Therefore, the ability of the NaK filter to bind both Na^+ and K^+ ions seemingly arises from ion's ability to utilize the existing environment in unique ways rather than any structural rearrangements of the filter itself.

Along with channel gating, the ability of ion channels to select for and allow the passage of specific ions through their conduction pores is central to their

physiological functioning [1]. Our knowledge of ion selectivity, as this process is known, has come a long way with the determination of several K^+ selective ion channel structures over the past decade [2,8,10,15,58,76]. However, several fundamental issues are yet to be fully understood and remain the focus of ongoing debate within the field. For example, is the snug-fit model alone enough to account for K^+ over Na^+ selectivity considering that protein 'breathing' itself can account for the difference in ionic radii or do ligand chemical environment (eight carbonyl oxygen atoms) and dynamics play the determinant role [7,77]?

The recently discovered NaK channel from *B. cereus* has provided a unique structural model for further probing mechanisms of ion selectivity compared to K^+ selective channels hitherto used as models for both selective and non-selective tetrameric cation channels. The channel shares overall structural similarities with KcsA but has been shown to conduct most group 1A cations as well as Ca^{2+}, using a unique mode of Ca^{2+} chelation with only backbone carbonyl oxygen atoms acting as ligands [3,5]. This ion non-selectivity is thought to arise from structural changes within the selectivity filter, where only the two most intracellular K^+ binding sites of KcsA (sites 3 and 4) are preserved while the upper two are replaced by a vestibular structure. Using the initial NaK structure, an analysis of structural differences among complexes of NaK and its various conducting ions has been difficult due to resolution limits as well as the presence of a high Ca^{2+} concentration in addition to monovalent cations in crystallization

conditions. To decipher the underlying mechanisms by which various monovalent cations are able to permeate NaK, we crystallized a truncated form of the channel, NaKNΔ19, previously used for channel function analysis. Well diffracting crystals were obtained and the structures were determined at resolutions ranging from 1.6 – 2.0 Å. The structure revealed the channel in an open conformation and a detailed analysis of gating mechanics was carried out and is presented in chapter 3. Here we use the high resolution structures of NaKNΔ19 in complex with various mono- and divalent cations to visualize the differences in ion binding profiles among various conducting ions at atomic detail. While our structural study reveals ion binding profiles in the NaK filter at atomic detail along with several interesting features that underlie NaK ion non-selectivity, fundamental questions remain about how sites with seemingly identical chemical environments can display different ion binding properties.

Na^+ binding in NaK selectivity filter

The structure of the NaKNΔ19-Na^+ complex was determined at 1.8 Å resolution and its $2F_o$-F_c ion omit map reveals three bound ions in the selectivity filter: in the vestibule, and sites 3 and 4 (Fig. 4.1a). The density in the vestibule and site 4 can be assigned to Na^+ ions but that at site 3 cannot, as will be discussed in detail later. The ion in the vestibule is coordinated by four carbonyl oxygen atoms of Val64s with a ligand-ion distance of about 2.9 Å. Four water molecules are clearly seen to reside within the vestibule, each with a distance of

about 4 Å to the Na^+ ion, suggesting no intimate interaction between the ion and the water molecules. It is interesting to note that the Na^+ ion in site 4 does not reside in the center of the ion binding cage formed by the hydroxyl and backbone carbonyl oxygen atoms from Thr63. Instead it sits in an almost planar conformation with respect to its ligands, namely the four hydroxyl oxygen atoms of Thr63s, with a distance of 2.4 Å. Furthermore, another water molecule in the central cavity, only seen in the Na^+ complex, also participates in Na^+ coordination with a Na^+-O distance of 2.7 Å. This scheme of pyramidal Na^+ coordination is reminiscent of what is seen in the Na^+ complex of the Guanine tetraplex structure [78], part of which is shown in figure 1b, drawn based on a 0.95 Å crystal structure of the complex. By using the O6 of the guanine base, the Guanine tetraplex generates a set of Na^+ binding sites that have a similar chemical environment as in NaK and K^+ channels (Fig. 4.6). Na^+ ions have a versatile way of binding and the one near the 3' end is planar with the tetrad and has a water molecule axial to it (Fig. 4.1b). The distance between Na^+ and O6 or water are in the range of 2.32 – 2.4 Å.

Identification of the bound ion at site 3 was complicated due to its apparent contamination by an unknown heavy atom ion or a mixture of ions. Even though 100mM NaCl was the only salt present in crystallization conditions, electron density at site 3 is too strong to be accounted for solely by Na^+ ions. The bound ion also carries an anomalous signal as shown in the anomalous difference

Fourier map (Fig. 4.7a). We suspect the source of this contamination is (±)-2-Methyl-2,4-pentanediol (MPD), used as a precipitant at high concentrations in the crystallization of NaKNΔ19 (Methods). MPD treatment with chelating resins carrying moieties for non-selective binding of both monovalent and divalent heavy metal ions can decrease the extent of contamination but, unfortunately, not eliminate it. Contamination from trace metal ions is not surprising judging from the very non selective nature of site 3, as will be discussed in further detail later. For simplicity, in our structural analysis we have assigned this strong density to Cs^+ and refined its occupancy to reveal the extent of the contamination. Even though the contamination obscures a direct visualization of possible Na^+ binding at site 3, important information can still be extracted from an analysis of electron density distribution. A $F_{low\ Na}$-$F_{high\ Na}$ difference map between NaKNΔ19 crystals grown in 100 mM NaCl (low Na) and those grown in 500 mM NaCl (high Na) reveals a strong peak at site 3, indicating the replacement of some contaminating heavy atoms by the less electron dense Na^+ ions (Fig. 4.7b). This is also evident from a decrease in ion occupancy of the heavy atoms (Cs^+ for the purpose of refinement) in the High Na^+ crystals. We therefore conclude that Na^+ does indeed bind at site 3 albeit at low affinity. From molecular dynamics studies, it has been suggested that Na^+ ions tend to bind at the upper or lower ends of the ion binding cage at site 3, almost planar with the backbone carbonyls of Val64 or Thr63 [79,80]. Three observations from NaKNΔ19 structures lead us to believe this

is actually the case. First, the football shaped electron density at site 3 in a $2F_o$-F_c ion omit map (Fig. 4.1c upper) indicates the presence of weak scattering elements at both end of the site. Second, a F_o-F_c difference map of the high Na^+ crystal reveals unexplained density on both ends of the site that likely comes from bound Na^+ ions (Fig. 4.1c, lower). This density is weak (4 sigma in figure 4.1c), as would be expected from a low occupancy and low scattering power of Na^+ ion. Finally, a similar planar conformation of a Na^+ ion with its ligand is observed at site 4. Thus, 3 distinct Na^+ binding positions are likely formed by sites 3 and 4 where the ions can be chelated in plane with their ligands (Fig. 4.1d), and the observed electron density in the filter is the combined effect of the ion distribution shown in figure 4.1 a & d.

K^+ & Rb^+ complex structures of NaKNΔ19

K^+- and Rb^+-complex structures of NaKNΔ19 were determined at 1.8 Å and 1.7 Å, respectively. While ion binding in the NaK filter is similar between both complexes, the details governing their ion chelation properties are noticeably different from the Na^+-complex. Both K^+ and Rb^+ display a strong preference for maintaining an octahedral arrangement of ligands. Figure 4.2 shows a $2F_o$-F_c ion omit map of the K^+(a) and Rb^+ (b) complex of NaKNΔ19, revealing four ion binding sites: the external entrance, vestibule, and sites 3 & 4. While no Na^+ binding was observed at the external entrance, K^+ and Rb^+ bind there in a half hydrated manner with the four carbonyl oxygen atoms from the Gly67 residues

and four water molecules acting as ligands. A half hydrated K^+ ion at a similar position has been observed in the KcsA structure[13]. However, the carbonyl oxygen atoms of Gly67, rather than pointing upwards as in KcsA, are oriented more inward, forming a better chelation scheme for K^+ and Rb^+. Half hydrated K^+ and Rb^+ ions are also observed in the vestibule of the filter chelated by the four carbonyl oxygen atoms of Val64 residues along with 4 water molecules. Thus, the involvement of water molecules allows for the maintenance of an octahedral ligand arrangement (Fig. 4.2c), mimicking the K^+ hydration shell also seen in KcsA [13]. It is important to note that these four water molecules are also seen within the vestibule of the filter in the Na^+ complex but, with ion-ligand distances of ~4 Å, are unlikely to be involved in ion chelation. K^+ and Rb^+ binding at sites 3 and 4 is virtually the same as that at equivalent sites in K^+ channels both in terms of position and ligand coordination. Heavy atom contamination at site 3 was still observed in the K^+ and Rb^+ complexes, but to a much lesser extent than in the Na^+ complex based on the following observation. A $F_{Na} - F_K$ difference map between crystals grown in 100 mM NaCl and KCl reveals strong electron density peak at site 3 (Fig. 4.8), despite K being a stronger X-ray scattering element than Na. This alludes to a competitive knockout of a larger fraction of the contaminating ion/ions by K^+, akin to a F_{heavy}-F_K map. This suggests that K^+ binds at site 3 better than Na^+. Taken together with the observation of K^+ binding at the external entrance, along with the functional

observation that K^+ has a larger effect on reducing ^{86}Rb influx into liposomes compared to Na^+ [5], it is reasonable to conclude that NaK is more selective for K^+ than Na^+.

Analysis of Cs^+ binding in NaK filter

Our analysis of monovalent cation binding in NaK was also extended to the larger Cs^+ ions. Even though we failed to produce crystals of NaKNΔ19 grown in 100 mM CsCl, the structure of a K^+ complex of NaKNΔ19 soaked in a stabilization solution containing 67 mM KCl and 33 mM CsCl (Methods) was determined at 1.8 Å resolution. The $F_{Cs\ soak} - F_K$ difference map between this soaked crystal and the native K^+ complex crystal revealed a strong peak at site 3 and two much weaker peaks in the vestibule (Fig. 4.2d). No K^+ replacement by Cs^+ was observed at the external entrance or site 4, indicating that Cs^+ appears to have a strong preference for site 3 with no detectable binding at the extracellular entrance and site 4 in the presence of K^+.

Divalent cation binding in the NaK filter

Although we were unable to crystallize NaKNΔ19 in $CaCl_2$ alone, we took advantage of the fact that no obvious Na^+ binding was observed at the external entrance in the Na^+-complex, and co-crystallized NaKNΔ19 in the presence of $CaCl_2$ in addition to 100 mM NaCl. In the presence of 10 mM Ca^{2+}, clear density corresponding to Ca^{2+} binding is observed at the external entrance in a $2F_o$-F_c ion omit map (Fig. 4.3a). To probe the binding affinity of Ca^{2+} at this site, we

performed a crystallographic titration assay by obtaining NaKNΔ19 crystals at different Ca^{2+} concentrations (0.5, 1.0, 2.5, 5.0 and 10 mM). Figure 3b shows two examples of the resulting difference maps between crystals with and without Ca^{2+} ($F_{0.5mM\ Ca^{2+}} - F_{0mM\ Ca^{2+}}$ and $F_{5mM\ Ca^{2+}} - F_{0mM\ Ca^{2+}}$), revealing stronger electron density from bound Ca^{2+} at the external site at higher [Ca^{2+}]. Since the only variable in crystallization conditions from which all crystals were obtained was the Ca^{2+} concentration and all diffraction data were scaled against that of the same native crystal, the difference in intensity of the electron density at the external entrance reflects the extent of Ca^{2+} binding, or occupancy, at the external site. Figure 4.3c shows a one-dimensional electron density profile corresponding to Ca^{2+} binding at the external entrance plotted along the central axis of the filter (Methods). An increase in Ca^{2+} occupancy is clearly seen with increasing Ca^{2+} concentrations. Crystals grown in 5 and 10 mM Ca^{2+} display a similar intensity of electron density, pointing to a saturation of Ca^{2+} binding at 10mM. This can be further verified by refining Ca^{2+} occupancy of the NaKNΔ19 co-crystallized with 10 mM Ca^{2+}, which gives rise to a value of 0.99. Assuming a spherical distribution of electron density from the bound Ca^{2+}, the integration of the area under each peak of the 1-D electron density profile and plotting these values against Ca^{2+} concentration (Fig. 4.3d) yields a K_d of 1.8 mM for the external site at pH 7.5 and in the presence of 100 mM Na^+, conditions under which the associated crystals were obtained. Ca^{2+} has also been shown to bind site 3

previously [3]. However its affinity cannot be determined by a similar titration assay because of competition from Na^+ and trace element binding at this site. Nevertheless Ca^{2+} binding at site 3 can be further confirmed by analyzing the effect of increasing Ca^{2+} concentration on the electron density profile at site 3. It is clear that increasing Ca^{2+} concentrations cause a corresponding decrease in electron density at this site, indicated by stronger peaks in the $F_{0\ Ca^{2+}}$-$F_{+\ Ca^{2+}}$ difference maps (Fig. 4.9). This points to an increase in the replacement of contaminating heavy atom by the lighter Ca^{2+} ions upon increasing Ca^{2+} concentrations.

Attempts at crystallizing NaKNΔ19 in the presence of Ba^{2+} also failed to yield high quality crystals. Consequently, we soaked a crystal of the K^+-complex of NaKNΔ19 in a stabilization solution containing 67 mM KCl and 33 mM $BaCl_2$ (see Methods) to analyze Ba^{2+} binding and determined its structure at 2.0 Å resolution. The $F_{Ba^{2+}\ soak} - F_K$ difference map between the Ba^{2+} soaked crystal and the native K^+ complex crystal confirms two Ba^{2+} binding positions, the external entrance and site 3, as was observed before[5] (Fig. 4.4a). Even though Ba^{2+} is present at half the concentration of K^+, refinement of the ion at the external site as Ba^{2+} in the soaked crystal gives rise to an occupancy of 0.97. This indicates an almost complete replacement of K^+ at the external site, suggesting a higher affinity for Ba^{2+} than K^+. Ba^{2+} coordination at the external site is similar to that of K^+ and Rb^+, with 4 water molecules forming a half hydration shell and 4 carbonyl

oxygen atoms of Gly67s serving as the other 4 ligands (Fig. 4.4b). This is different from Ca^{2+} binding, where no hydration shell was observed in external Ca^{2+} chelation (Fig. 4.3a). This does not necessary mean that water molecules do not participate in external Ca^{2+} chelation. It could simply be that because Ca^{2+} prefers 6 or 7 ligands as in other Ca^{2+} binding motifs like the EF-hand [48,49,81], the symmetry mismatch between the channel and the configuration of Ca^{2+} chelation leads to a 4-fold reduction of occupancy of the water molecules. It is also interesting to note that even though sites 3 & 4 in KcsA have a virtually identical chemical environment as the corresponding sites in NaK, Ba^{2+} only binds site 3 in NaK instead of site 4 as in KcsA.

Although we were unable to carry out an analysis of Ba^{2+} affinity at both sites, we expect it to be fairly high for at least one of them based on results from ^{86}Rb flux assays. Figure 4c shows an analysis of Ca^{2+} and Ba^{2+} blocking of ^{86}Rb influx in liposomes loaded with NaCl. It is clear that Ba^{2+} displays much stronger concentration dependent blocking of ^{86}Rb influx compared to Ca^{2+} (Fig. 4.4c).

Discussion

The four well defined ion binding sites in the NaK filter can be divided into three subtypes based on the nature of their ligands: carbonyl-water for the external site and vestibule, carbonyl-carbonyl for site 3, and carbonyl-hydroxyl for site 4. Despite their similar chemical environments, these sites display a different ion binding preference as summarized in Table 4.1.

The external site, formed by 4 carbonyl oxygen atoms from Gly 67 along with extracellular water molecules can bind both mono (K^+ and Rb^+) and divalent (Ca^{2+} and Ba^{2+}) cations. Interestingly, no obvious Na^+ binding was observed at this site. This site is interesting in its apparently greater selectivity for divalent cations, which arises from the through space interaction between Asp66 and the Gly67-Asn68 peptide bond as reported previously [3]. The Ca^{2+} affinity at this site has been calculated to be 1.8mM from our crystallographic titration experiment.

With the involvement of four water molecules, the position of ion binding in the vestibule of the NaK selectivity filter is equivalent to that of site 2 in KcsA. However, the mobility of the water molecules imparts greater flexibility in ion binding, allowing the site to accommodate various monovalent cations (Na^+, K^+, Rb^+). Thus, even though the highly K^+ selective sites 1 & 2 of K^+ channels are absent, the channel is still equipped for optimal K^+ conduction through the use of water molecules that help create a ligand arrangement mimicking the K^+ hydration shell. These four water molecules have longer ion-water distances in the Na^+-complex than K^+-complex and do not form a hydration shell around Na^+ ions. This might be a consequence of Na^+ having a much smaller radius than K^+ and Rb^+, which could spatially prevent an octahedral arrangement of ligands for Na^+ coordination.

Sites 3 and 4 in NaK are virtually identical to those in K^+ channels in terms of structure and ligand type as shown in the superimposition of their

selectivity filter regions (Fig 4.5a). However, they exhibit vastly different ion binding properties. Site 3 in NaK is of particular interest as it appears to be the most non-selective, accommodating both mono- and divalent cations with wide ranging radii, making it it inevitably susceptible to contamination from trace elements. Three major differences in ion binding at sites 3 and 4 between NaK and K^+ channels are obvious. First, Ba^{2+}, a well known K^+ channel blocker [82-85], binds at site 4 in K^+ channels but at site 3 in NaK. Second, Cs^+ can bind at both sites in K^+ channels but prefers to bind at site 3 in NaK in the presence of K^+. Finally, while Na^+ binds at both sites in NaK, no Na^+ binding was observed in K^+ channels. In light of no obvious structural differences in sites 3 and 4 between NaK and K^+ channels, these differences in Ba^{2+} and Cs^+ binding are intriguing and the underlying features that give rise to them require further investigation.

The unique ability of the NaK selectivity filter to utilize water molecules in sync with carbonyl oxygen atoms has important consequences for ion chelation. The ability to form octahedral ion chelation schemes seemingly makes the NaK selectivity filter more optimized for K^+ binding than Na^+. This hypothesis is supported by data from competition assays where externally added K^+ has a more pronounced effect on reducing ^{86}Rb accumulation in liposomes compared to Na^+ [5]. However, this K^+ over Na^+ selectivity in NaK clearly does not occur to the same extent as in K^+ channels and NaK is able to conduct Na^+ well. Overall, we believe two factors may be key contributors to the ion selectivity

differences observed between NaK and K^+ channels. The first is the apparent need for K^+ ions to stabilize the selectivity filter of K^+ channels in the 'conducting' state. Replacement of K^+ with Na^+ leads to a 'collapsed' filter which yields the channel non conductive [86]. Such a dependence on K^+ ions for maintaining the structural integrity of the selectivity filter is not observed in the NaK channel, which maintains an almost identical structure in complex with Na^+, K^+, or Rb^+ as shown in figure 4.5b. It is worth noting that the presence of contaminating ions at site 3 makes it difficult to make any definitive assertions regarding subtle structural differences in the NaK selectivity filter. However, it is still clear that major rearrangements do not occur upon binding of different ions, as a mixture of proteins with two conformations at the filter region is not expected to yield well diffracting crystals. The structural stability of the NaK selectivity filter can be partly attributed to strong H-bonding interactions between Asp66 and the backbone amide of Asn68. Another cause could be related to how well Na^+ ions bind within the selectivity filter. In a recent study, mutation of a conserved Glycine (Gly77) residue to D-Ala in KcsA yielded a channel that maintained a conductive selectivity filter even in the presence of Na^+ [87]. The mutant channel can conduct Na^+ but is still very selective for K^+, suggesting that the 4 equivalent K^+ binding sites in a K^+ channel selectivity filter are not energetically favorable for Na^+ binding. The replacement of K^+ channel sites 1&2 with a water-filled vestibule in NaK may overcome this energy barrier and make Na^+ binding less

unfavorable. Na^+ ions display versatility in relative positioning and number of ligands, as shown in the NaKNΔ19-Na^+ complex. Ions are not restricted to the middle of the ion binding sites, but bind at the upper and lower edges instead, in plane with 4 carbonyl or hydroxyl oxygen atoms. A well ordered water molecule in the cavity just below the selectivity filter participates in a pyramidal Na^+ chelation scheme for an ion in site 4 as seen in the guanine tetraplex structure as mentioned earlier. This could very well be the case for a Na^+ ion at site 3 as the ion could be stabilized by a water molecule in the vestibule. Therefore, by having partial exposure to solvent, Na^+ can bind both at site 3 and 4 in a favorable configuration as has been suggested previously[80].

Methods

Detailed experimental procedures are the same as described in our companion paper. Na^+, K^+, and Rb^+ complexes of NaKNΔ19 were purified with the corresponding salts (100 mM NaCl, KCl or RbCl) and crystallized over a well solution containing 55-70% (±)-2-Methyl-2,4-pentanediol (MPD) and 100mM Hepes pH 7.5. All crystals used for the Ca^{2+} titration assay were obtained by using proteins purified in 100 mM NaCl and with the addition of 0.5-10mM $CaCl_2$ to the crystallization well solution. For soaking experiments, crystals of the NaKNΔ19-K^+ complex were soaked in stabilization solutions containing 67 mM KCl and 33 mM CsCl or $BaCl_2$ for one day.

A majority of the crystals suffered from either partial or perfect twinning [88]. Several data sets were therefore collected for each of the structures reported here and in our companion study to obtain at least one untwinned data set of high quality. The only exception was the data set collected for NaKND19-Rb^+ complex, which has a twinning fraction of 20% and was detwinned in CCP4 [73] before being used for refinement. All statistics of data collection and refinements are listed in Table I of our companion paper.

One dimensional electron density profiles of external Ca^{2+} binding were obtained as described [89]. All data from Na^+ complexes co-crystallized with 0.5 – 10 mM Ca^{2+} were scaled to 2.1 Å using the native NaKND19-Na^+ crystal (without Ca^{2+}) as a reference. 1-D profiles were obtained by sampling the $F_{0.5\text{-}10mM\ Ca}$-$F_{0mM\ Ca}$ difference maps along the z/central axis at the external site using MAPMAN [90]. Ion occupancy was obtained by integrating the area under each peak on the 1-D profile and normalizing it against that of the 10 mM Ca^{2+} peak.

The divalent cation (Ca^{2+} and Ba^{2+}) blockage of the NaK channel was studied by analyzing the competing effect of Ca^{2+} and Ba^{2+} in ^{86}Rb flux assay. In this competition assay, the tested ions (Ca^{2+} and Ba^{2+}) were added directly into the flux buffer at appropriate concentrations to give the desired final concentrations upon addition of liposomes. Ion flux was then allowed to proceed for 10 minutes before radioactivity levels were counted as described.

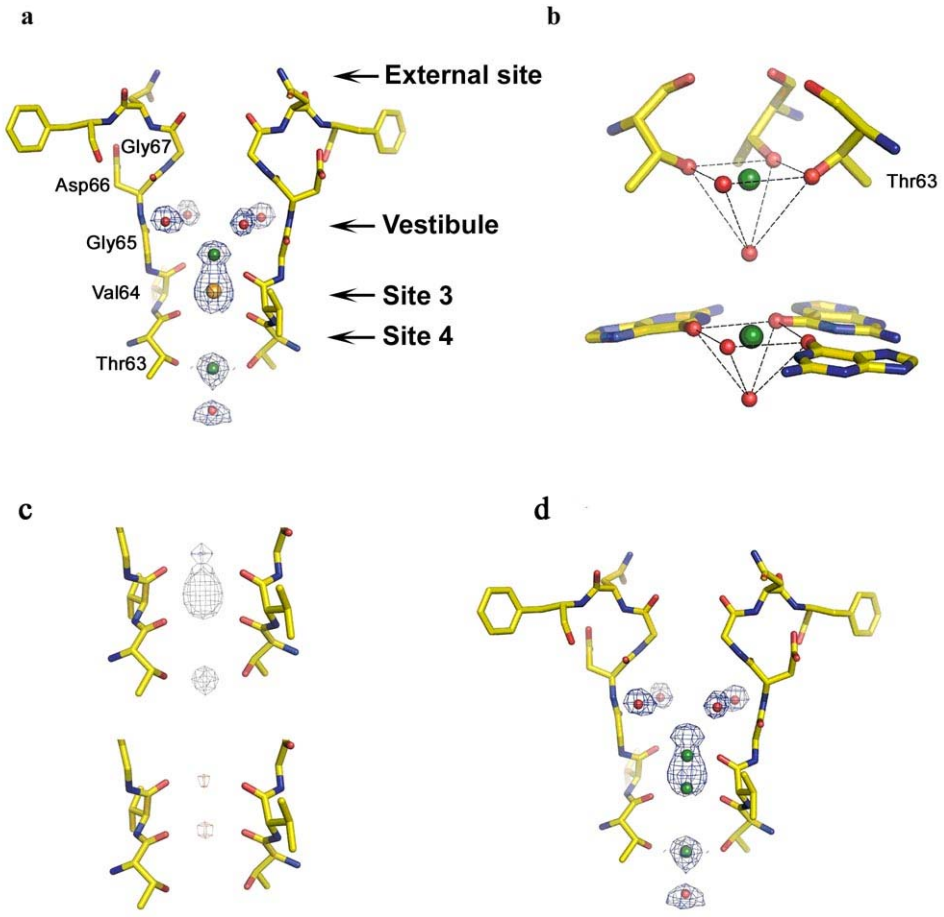

Figure 4.1 Na^+ binding in the NaK filter **a)** $2F_o$-F_c ion omit map contoured at 1.5σ showing density (blue mesh) for Na^+ ions, water molecules in the vestibule and central cavity, and the contaminating ion at site 3 (green, red, and orange spheres, respectively). The front and back subunits of the NaK model have been removed for clarity in most figures. **b)** Comparison of Na^+ binding in NaK at site 4 (upper) and the 3' side of the guanine tetraplex (lower) showing Na^+ binding in plane with 4 of its ligand, with a water molecule sitting axial to it. **c)** $2F_o$-F_c ion omit map contoured at 2.5σ (blue mesh, upper) showing football shape of electron density at site 3 of NaKNΔ19 in high Na^+ (500mM); and the F_o-F_c map with Cs^+ at site 3 contoured at 4 σ (red mesh, lower) showing density that likely arises from a contribution of Na^+ present on both the upper and lower edges of site 3. **d)** Suggested mode of Na^+ binding at the upper and lower edges of site 3.

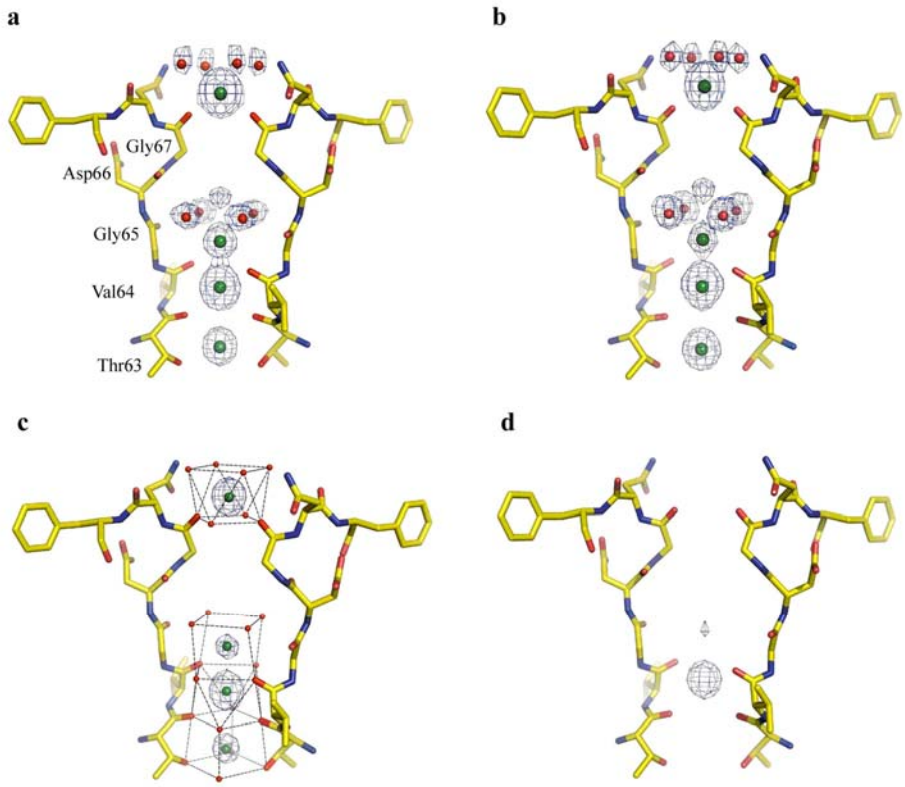

Figure 4.2 K^+ and Rb^+ binding in the NaK selectivity filter. The $2F_o$-F_c ion omit maps (1.5σ) show electron density of ion binding in the K^+ complex (a) and Rb^+ complex **(b)** of NaKNΔ19. K^+ and Rb^+ ions are colored green with water molecules represented as red spheres. **c)** The maintenance of an octahedral ligand arrangement in the K^+ complex, which also holds true for the Rb^+ complex. The oxygen ligand from the front and back subunits are shown as red spheres. **d)** $F_{Cs\ soak} - F_K$ difference map contoured at 10 σ showing Cs^+ binding at site 3.

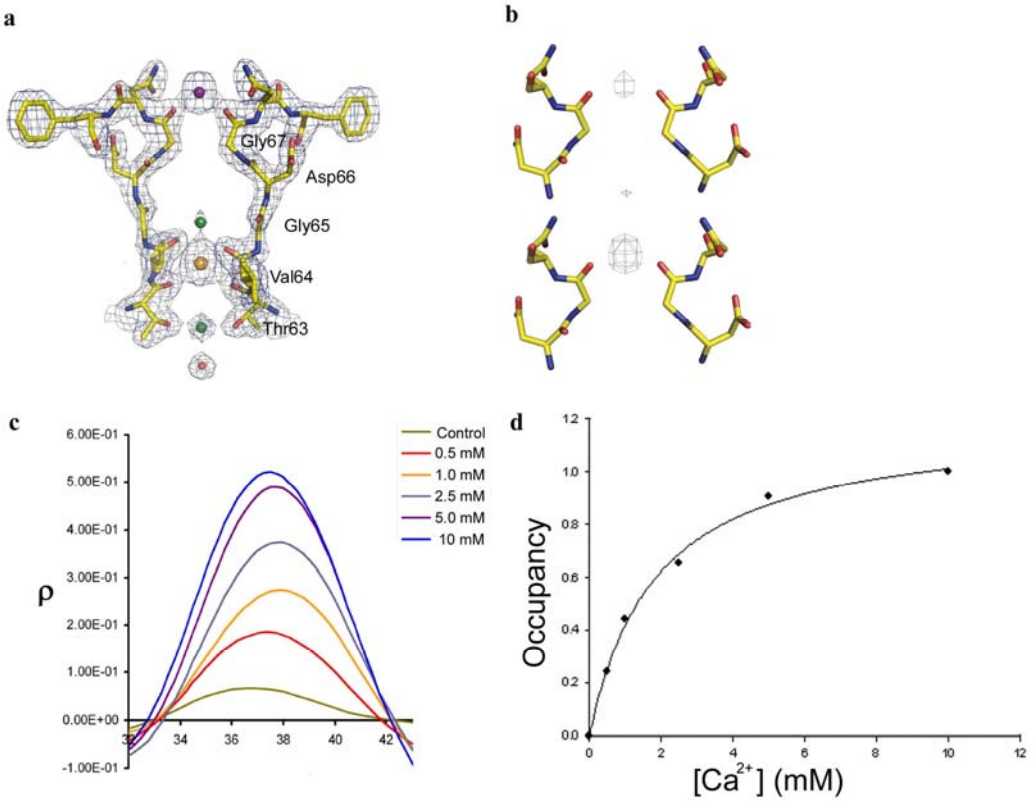

Figure 4.3 Ca^{2+} binding in the NaK selectivity filter. **(a)** $2F_o$-F_c ion omit map (1.5σ) of the NaKNΔ19-Na^+ complex co-crystallized with 10mM $CaCl_2$, showing electron density for a Ca^{2+} ion (purple sphere) at the external entrance. Na^+ and the contaminant at site 3 are modeled as green and orange spheres, respectively. Electron density for the protein backbone is also shown as a blue mesh. **(b)** $F_{0.5mM\ Ca} - F_{0mM\ Ca}$ (upper) and $F_{5mM\ Ca^{2+}} - F_{0mM\ Ca^{2+}}$ (lower) difference map contoured at 10 σ showing increasing intensity of Ca^{2+} binding upon increasing Ca^{2+} concentration. Dotted lines indicate the position of central axis along which the 1-D electron density was calculated. **(c)** 1-D electron density profile of Ca^{2+} binding at the external entrance showing increased Ca^{2+} binding at increasing concentrations. The control is from a difference map between two native crystals grown in the absence of Ca^{2+}. **(d)** Occupancy of Ca^{2+} binding at the external site was calculated by integration of the peaks in 1-D electron density profile and normalizing them against the 10 mM Ca^{2+} peak. The plot of occupancy against Ca^{2+} concentration give rise to a K_d value of about 1.8 mM upon fitting the curve to a single component langmuir equation.

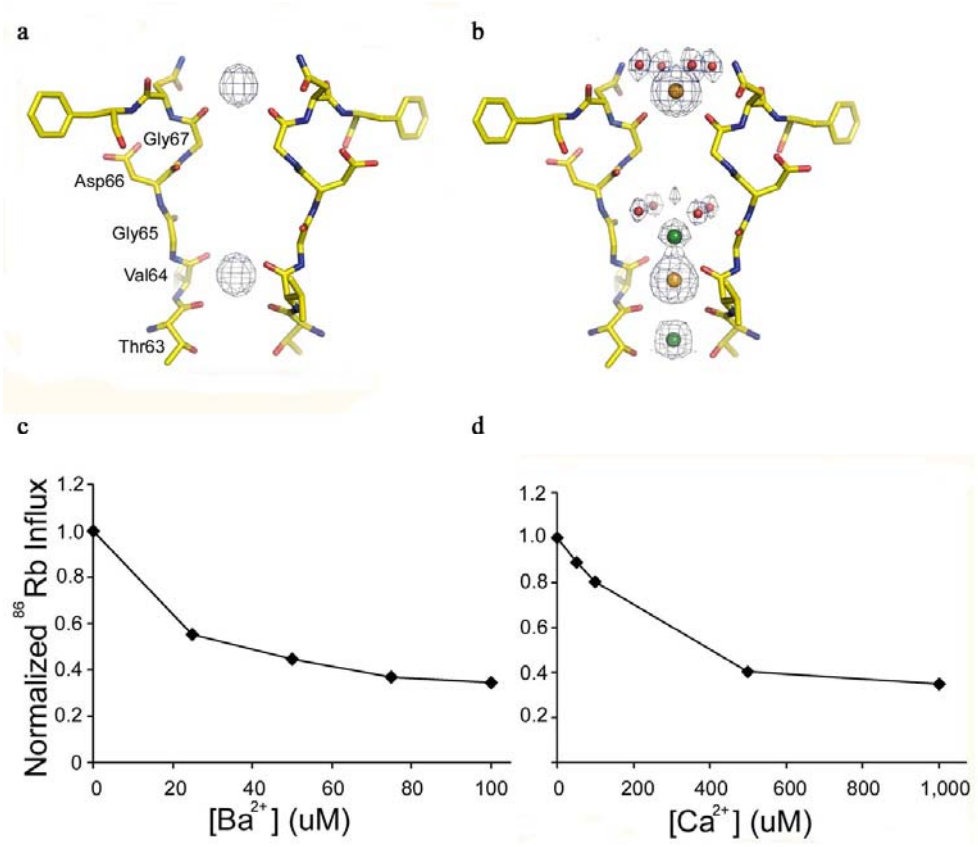

some

Figure 4.4 Ba^{2+} binding in NaK filter. a) $F_{Ba\ soak} - F_K$ difference map (blue mesh) contoured at 10 σ showing the two Ba^{2+} binding sites. (b) $2F_o$-F_c ion omit maps of Ba^{2+}-soaked crystal contoured at 1.5 σ. The electron density at external entrance and site 3 was modeled as Ba^{2+} (orange spheres) and water molecules are modeled as red spheres. (c) Ba^{2+} (left) and Ca^{2+} (right) blocking of ^{86}Rb influx in liposomes loaded with NaCl.

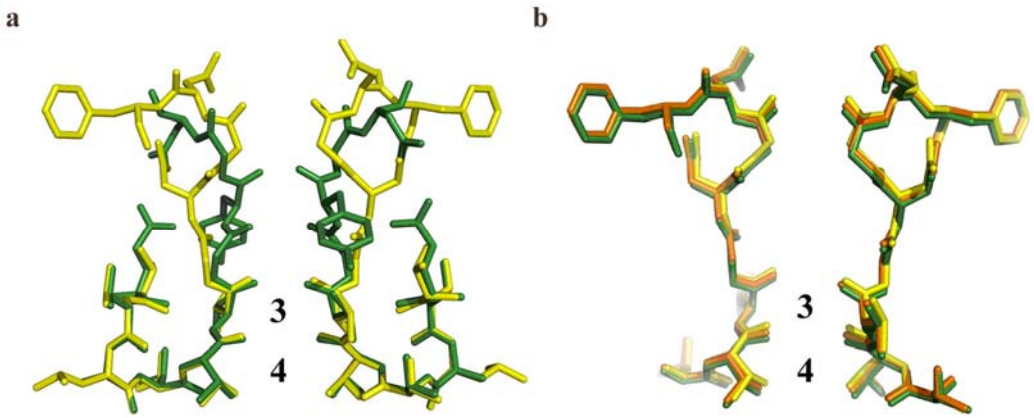

Figure 4.5 Comparison of the selectivity filter structures of NaK and KcsA and between various ion complexes of NaK. **a)** Superimposition of the NaK selectivity filter (yellow) in complex with K^+ with that of KcsA (green, PDB code 1K4C). **b)** Superimposition of the selectivity filters of the NaKNΔ19 channel in complex with Na^+ (yellow), K^+ (green), and Rb^+ (orange).

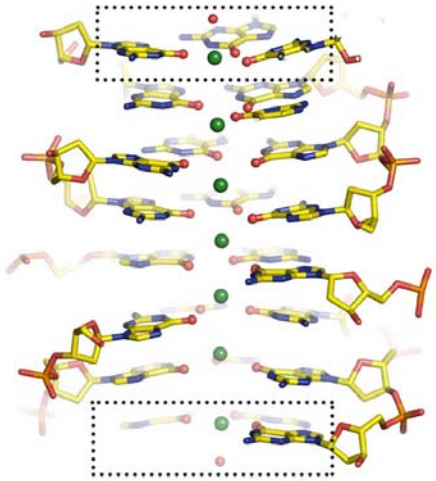

Figure 4.6 Partial structure of the Guanine tetraplex (PDB code 244d). Na^+ ions and water molecules are modeled as green and red spheres, respectively. The boxed regions highlight 3' ion binding sites displaying 3 of the 4 O6 atoms chelating Na^+ ions with one water molecule positioned axial to it. A zoom in view of the lower boxed region was shown in the main text (Fig. 1b)

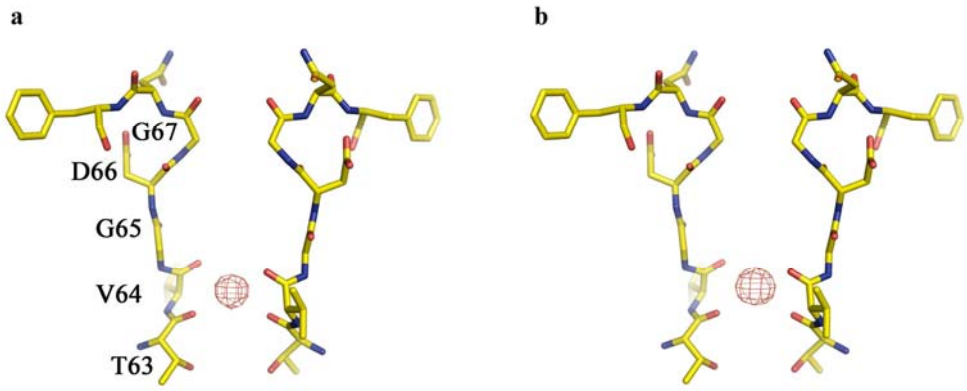

Figure 4.7 Contamination of site 3 in the NaK filter by unknown heavy atom ion or mixture of ions. **a)** F_+-F_- anomalous difference map contoured at 12σ (red mesh) showing anomalous signal originating from a contaminating heavy atom ion. **b)** $F_{low\ Na}$-$F_{high\ Na}$ difference map contoured at 12 σ (Red mesh) between crystals grown in 100mM and 500mM NaCl.

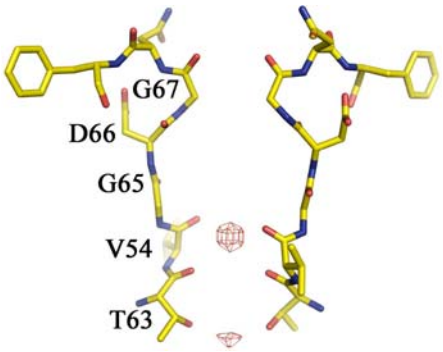

Figure 4.8 F_{Na} – F_K difference map contoured at 12σ (red mesh) between the NaK-Na^+ and NaK-K^+ complexes revealing a lesser extent of contamination in the K^+ complex.

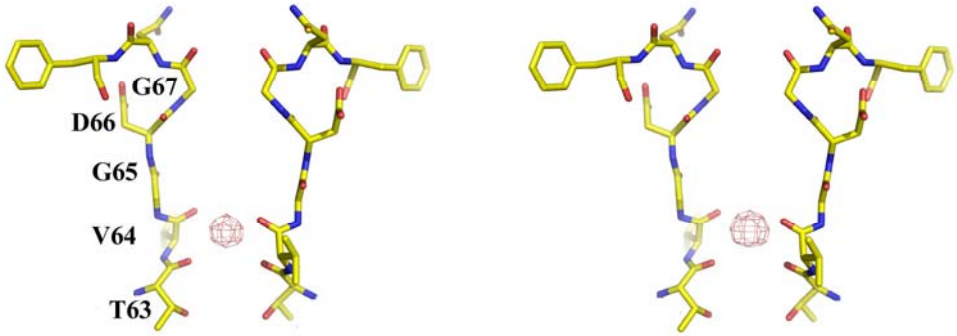

Figure 4.9 $F_{0\ mM\ Ca^{2+}}$-$F_{1\ mM\ Ca^{2+}}$ (left) and $F_{0\ mM\ Ca^{2+}}$-$F_{10\ mM\ Ca^{2+}}$ (right) displaying stronger electron density peaks at site 3 with increasing [Ca^{2+}].

Table 4.1 Ion Binding Properties of individual Sites In the NaK Selectivity Filter

Site	Ligand Type	Ion-ligand distance (Å)					Selectivity
		Na^+	K^+	Rb^+	Ba^{2+}	Ca^{2+}	
External	H_2O C=O (Gly67)		3.06 2.52	2.77 2.50	2.94 2.73	2.43	K^+, Rb^+, Ca^{2+}, Ba^{2+}
Vestibule	H_2O C=O (Val64)	4.02 2.94	2.96 3.00	2.85 3.11			Na^+, K^+, Rb^+
Site 3	C=O (Val64) C=O (Thr63)		2.80 2.83	2.97 2.94			Na^+, K^+, Rb^+, Cs^+, Ca^{2+}, Ba^{2+}, others*
Site 4	C=O (Thr63) -OH (Thr63)	2.38	2.97 2.79	2.98 2.89			Na^+, K^+, Rb^+

*refers to unknown contaminating ions.

Table 4.2 Data collection and refinement statistics for NaKNΔ19 in complex with various cations.

NaKNΔ19-complex Conentrations (mM)	Na^+ 100	Na^+ 500	K^+ 100	Rb^+ 100	Na^+/Ca^{2+} 100/10	K^+/Ba^{2+} 67/33
Data collection						
Space group	I4	I4	I4	I4	I4	I4
Cell dimensions						
a=*b*(Å)	68.050	68.056	68.194	68.134	67.990	68.226
c (Å)	89.251	89.326	89.294	89.359	89.168	89.548
Resolution (Å)	50 - 1.8	50 - 1.8	50 - 1.8	50 - 1.7	50 - 2.0	50 - 2.0
R_{sym} (%)	5.1 (65.5)	6.4 (82.1)	4.9 (56)	6.2 (59.9)	5.7 (34.3)	8.4 (60.4)
I/σI	36 (2)	30 (1.5)	41 (2)	31 (2)	38 (2.5)	26 (2.0)
Completeness (%)	99.3(99.3)	99.6(99.7)	99.6(99.6)	96.6(71.3)	97.2(81.6)	99.9(99.4)
Redundancy	6.8 (5.9)	6.8 (5.4)	7.0 (5.1)	6.8 (4.4)	6.6 (4.7)	6.9 (5.1)
Refinement						
Resolution (Å)	1.8.	1.8	1.8	1.7	2.0	2.0
No. Reflections	18808	18965	18948	21705	13398	13987
R_{work} / R_{free}	21.3/24.8	21.5/23.6	21.2/23.4	22.0/22.9	20.0/23.5	20.1/24.8
No. atoms						
Protein	1462	1462	1462	1462	1462	1462
MPD/ Ion	24/6	0/5	32/10	32/11	24/8	16/10
Water	144	111	96	94	52	57
B-factors						
Protein	37.60	36.06	34.692	30.583	49.385	39.206
Ligand/ion	49.03	30.592	50.317	51.79	67.043	51.841
Water	60.855	56.592	53.276	47.63	70.243	54.492
R.m.s.d						
Bond lengths (Å)	0.0060	0.0084	0.0053	0.0059	0.0062	0.0060
Bond angles (°)	1.089	1.260	1.070	1.116	1.099	1.068

*Values in parentheses are for highest-resolution shell.

DISCUSSION

Judging from their prevalence in and importance to nearly all living cells, ion channels are undoubtedly among the most important biological machines. It comes as no surprise that ion channel dysfunction lies at the center of numerous diseases, including several serious human conditions such as different types of seizures, ataxia, various heart conditions, and even certain forms of diabetes and vascular diseases[91]. Like any other integral membrane proteins, however, the biochemical characterization of ion channels remains a challenging task owing to inherent difficulties in obtaining pure and stable samples. Electrophysiologists have historically been at the center of tackling functional characterization, generating a vast amount of information for various transport proteins. However, studies characterizing the molecular details underlying important ion channel properties, apart from mutagenesis and functional analyses pinpointing important residues or motifs, remain lacking. An exception to this is the family of K^+ selective channels for which a large body of structural work has offered a tremendous amount of detailed information about the atomic details that underlie fundamental channel properties like ion selectivity and gating.

The successful over-expression, purification, and eventual crystallization and structure determination of several K^+ channels by the Mackinnon lab over the last decade has opened the door for structural-function studies on ion channels employing the powerful and tested combination of crystallographic and electrophysiological tools. This was largely made possible due to the use of prokaryotic K^+ channels, shown by sequence

analysis and later confirmed by structures of eukaryotic channels to be reasonably accurate models for their eukaryotic counterparts.

The use of bacterial homologs as structural models for more complex systems has been gaining popularity over the last few years. Consequently, structure-function studies on membrane proteins comprising actual three-dimensional structures have become more commonplace. Additionally the structures of several bacterial ion transporters not belonging to the tetrameric cation channel family have also been determined. The caveats and criticisms of this approach center around the accuracy of bacterial model systems, especially when fitting the results gathered in the framework of the candidate protein's physiological role in its native environment. Nonetheless, it is difficult to argue that these model systems have opened up a new avenue to tackle questions long thought of as too challenging to address.

The structure of NaK was the first for a channel able to conduct both K^+ and Na^+. A single amino acid change in the selectivity filter has been proposed to be the underlying factor but, as mentioned previoulsy, mutation of the TVGDG signature sequence of NaK to the K^+ channel TVGYG sequence itself failed to convert NaK into a K^+ selective channel. One can therefore argue the merits of using the NaK selectivity filter as a model for those of CNG channels which, based on the sequence alignments shown previously, tend to be one residue shorter. An acceptance of this, however, in no way diminishes our findings for a number of reasons. First, the NaK structures have shown conclusively that selectivity filters capable of specifically binding and conducting Ca^{2+}, like those of CNG and Ca^{2+} channels, can indeed be lined predominantly with backbone carbonyl oxygen atoms. Second, the observation of the gating hinge glycine in

NaK, other prokaryotic and eukaryotic K^+ channels, as well as CNG channels points to a similar pore opening mechanism. Our conclusions in regards to the ion binding in NaK are based on observed electron density profiles. The high resolution structures of the open NaK channel allowed for the visualization of key features, including the utilization of ordered water molecules to create K^+ binding sites similar to those seen in KcsA. Therefore, a discussion of our findings in terms of an extension to CNG or Ca^{2+} channels necessitates a clear demarcation of the kind of information one seeks to obtain. In other words it is unreasonable to suggest that NaK, as a structural model, can accurately represent or predict variables like absolute ion binding affinities, levels of selectivity, etc., for each of the different channels we have drawn parallels to. What it does do, however, is fit the framework of underlying themes seen time and time again for ion selectivity and pore opening that, in general terms, likely hold true for other systems. Additionally, these structures provide valuable starting points for structure based mutagenesis studies on their eukaryotic counterparts for which no structures are available.

The ultimate validation for how accurate a structural model NaK is for ion selectivity and gating in eukaryotic channels will come with the structure determination of channels like CNG, Ca^{2+} and Na^+ selective ones. Already a growing body of work detailing expression and purification of eukaryotic membrane proteins from mammalian, insect, or yeast cells has appeared in the literature. The logical follow up to this project, aside from mutagensis studies seeking to make the current models more accurate representation of specific systems, is a transition from bacterial systems to eukaryotic ones. A beautiful example of this, already discussed previously, is the recent structure

determination of the mammalian voltage dependent K+ channel[76,92]. I believe structures of real CNG channels, obtained using similar methods are not far from reach and have already begun setting up yeast expression systems that will allow us to focus directly on eukaryotic proteins.

REFERENCES

1. Hille, B. *Ion Channels of Excitable Membranes*, (Sinauer Associates, Inc., Sunderland, MA, 2001).
2. Long, S.B., Tao, X., Campbell, E.B. & MacKinnon, R. Atomic structure of a voltage-dependent K+ channel in a lipid membrane-like environment. *Nature* **450**, 376-82 (2007).
3. Alam, A., Shi, N. & Jiang, Y. Structural insight into Ca2+ specificity in tetrameric cation channels. *Proc Natl Acad Sci U S A* **104**, 15334-9 (2007).
4. Ye, S., Li, Y., Chen, L. & Jiang, Y. Crystal Structures of a Ligand-free MthK Gating Ring: Insights into the Ligand Gating Mechanism of K(+) Channels. *Cell* **126**, 1161-73 (2006).
5. Shi, N., Ye, S., Alam, A., Chen, L. & Jiang, Y. Atomic structure of a Na+- and K+-conducting channel. *Nature* **440**, 570-4 (2006).
6. Long, S.B., Campbell, E.B. & Mackinnon, R. Crystal structure of a mammalian voltage-dependent Shaker family K+ channel. *Science* **309**, 897-903 (2005).
7. Gouaux, E. & Mackinnon, R. Principles of selective ion transport in channels and pumps. *Science* **310**, 1461-5 (2005).
8. Kuo, A. et al. Crystal structure of the potassium channel KirBac1.1 in the closed state. *Science* **300**, 1922-6 (2003).
9. Jiang, Y., Ruta, V., Chen, J., Lee, A. & MacKinnon, R. The principle of gating charge movement in a voltage-dependent K+ channel. *Nature* **423**, 42-8 (2003).
10. Jiang, Y. et al. X-ray structure of a voltage-dependent K+ channel. *Nature* **423**, 33-41 (2003).
11. Dutzler, R., Campbell, E.B. & MacKinnon, R. Gating the selectivity filter in ClC chloride channels. *Science* **300**, 108-12 (2003).
12. Doyle, D.A. et al. The structure of the potassium channel: molecular basis of K+ conduction and selectivity. *Science* **280**, 69-77 (1998).
13. Zhou, Y., Morais-Cabral, J.H., Kaufman, A. & MacKinnon, R. Chemistry of ion coordination and hydration revealed by a K+ channel-Fab complex at 2.0 A resolution. *Nature* **414**, 43-8 (2001).
14. Jiang, Y. et al. Crystal structure and mechanism of a calcium-gated potassium channel. *Nature* **417**, 515-22 (2002).
15. Jiang, Y. et al. The open pore conformation of potassium channels. *Nature* **417**, 523-6 (2002).
16. MacKinnon, R. Determination of the subunit stoichiometry of a voltage-activated potassium channel. *Nature* **350**, 232-5 (1991).

17. MacKinnon, R. Using mutagenesis to study potassium channel mechanisms. *J Bioenerg Biomembr* **23**, 647-63 (1991).
18. MacKinnon, R. New insights into the structure and function of potassium channels. *Curr Opin Neurobiol* **1**, 14-9 (1991).
19. Yellen, G., Jurman, M.E., Abramson, T. & MacKinnon, R. Mutations affecting internal TEA blockade identify the probable pore-forming region of a K+ channel. *Science* **251**, 939-42 (1991).
20. Zhou, Y. & MacKinnon, R. Ion binding affinity in the cavity of the KcsA potassium channel. *Biochemistry* **43**, 4978-82 (2004).
21. Zhou, M. & MacKinnon, R. A mutant KcsA K(+) channel with altered conduction properties and selectivity filter ion distribution. *J Mol Biol* **338**, 839-46 (2004).
22. Valiyaveetil, F.I., Sekedat, M., Muir, T.W. & MacKinnon, R. Semisynthesis of a functional K+ channel. *Angew Chem Int Ed Engl* **43**, 2504-7 (2004).
23. Valiyaveetil, F.I., Sekedat, M., Mackinnon, R. & Muir, T.W. Glycine as a D-amino acid surrogate in the K(+)-selectivity filter. *Proc Natl Acad Sci U S A* **101**, 17045-9 (2004).
24. Sather, W.A. & McCleskey, E.W. Permeation and selectivity in calcium channels. *Annu Rev Physiol* **65**, 133-59 (2003).
25. Lu, Z., Klem, A.M. & Ramu, Y. Ion conduction pore is conserved among potassium channels. *Nature* **413**, 809-13 (2001).
26. LeMasurier, M., Heginbotham, L. & Miller, C. KcsA: it's a potassium channel. *J Gen Physiol* **118**, 303-14 (2001).
27. MacKinnon, R., Cohen, S.L., Kuo, A., Lee, A. & Chait, B.T. Structural conservation in prokaryotic and eukaryotic potassium channels. *Science* **280**, 106-9 (1998).
28. Yau, K.W. & Baylor, D.A. Cyclic GMP-activated conductance of retinal photoreceptor cells. *Annu Rev Neurosci* **12**, 289-327 (1989).
29. Kaupp, U.B. & Seifert, R. Cyclic nucleotide-gated ion channels. *Physiol Rev* **82**, 769-824 (2002).
30. Matulef, K. & Zagotta, W.N. Cyclic nucleotide-gated ion channels. *Annu Rev Cell Dev Biol* **19**, 23-44 (2003).
31. Zagotta, W.N. & Siegelbaum, S.A. Structure and function of cyclic nucleotide-gated channels. *Annu Rev Neurosci* **19**, 235-63 (1996).
32. Baumann, A., Frings, S., Godde, M., Seifert, R. & Kaupp, U.B. Primary structure and functional expression of a Drosophila cyclic nucleotide-gated channel present in eyes and antennae. *Embo J* **13**, 5040-50 (1994).
33. Finn, J.T., Solessio, E.C. & Yau, K.W. A cGMP-gated cation channel in depolarizing photoreceptors of the lizard parietal eye. *Nature* **385**, 815-9 (1997).

34. Frings, S., Seifert, R., Godde, M. & Kaupp, U.B. Profoundly different calcium permeation and blockage determine the specific function of distinct cyclic nucleotide-gated channels. *Neuron* **15**, 169-79 (1995).
35. Hackos, D.H. & Korenbrot, J.I. Divalent cation selectivity is a function of gating in native and recombinant cyclic nucleotide-gated ion channels from retinal photoreceptors. *J Gen Physiol* **113**, 799-818 (1999).
36. Picones, A. & Korenbrot, J.I. Permeability and interaction of Ca2+ with cGMP-gated ion channels differ in retinal rod and cone photoreceptors. *Biophys J* **69**, 120-7 (1995).
37. Haynes, L.W., Kay, A.R. & Yau, K.W. Single cyclic GMP-activated channel activity in excised patches of rod outer segment membrane. *Nature* **321**, 66-70 (1986).
38. Stern, J.H., Knutsson, H. & MacLeish, P.R. Divalent cations directly affect the conductance of excised patches of rod photoreceptor membrane. *Science* **236**, 1674-8 (1987).
39. Colamartino, G., Menini, A. & Torre, V. Blockage and permeation of divalent cations through the cyclic GMP-activated channel from tiger salamander retinal rods. *J Physiol* **440**, 189-206 (1991).
40. Zimmerman, A.L. & Baylor, D.A. Cation interactions within the cyclic GMP-activated channel of retinal rods from the tiger salamander. *J Physiol* **449**, 759-83 (1992).
41. Seifert, R., Eismann, E., Ludwig, J., Baumann, A. & Kaupp, U.B. Molecular determinants of a Ca2+-binding site in the pore of cyclic nucleotide-gated channels: S5/S6 segments control affinity of intrapore glutamates. *Embo J* **18**, 119-30 (1999).
42. Root, M.J. & MacKinnon, R. Identification of an external divalent cation-binding site in the pore of a cGMP-activated channel. *Neuron* **11**, 459-66 (1993).
43. Eismann, E., Muller, F., Heinemann, S.H. & Kaupp, U.B. A single negative charge within the pore region of a cGMP-gated channel controls rectification, Ca2+ blockage, and ionic selectivity. *Proc Natl Acad Sci U S A* **91**, 1109-13 (1994).
44. Gavazzo, P., Picco, C., Eismann, E., Kaupp, U.B. & Menini, A. A point mutation in the pore region alters gating, Ca(2+) blockage, and permeation of olfactory cyclic nucleotide-gated channels. *J Gen Physiol* **116**, 311-26 (2000).
45. Karpen, J.W., Brown, R.L., Stryer, L. & Baylor, D.A. Interactions between divalent cations and the gating machinery of cyclic GMP-activated channels in salamander retinal rods. *J Gen Physiol* **101**, 1-25 (1993).

46. Dzeja, C., Hagen, V., Kaupp, U.B. & Frings, S. Ca2+ permeation in cyclic nucleotide-gated channels. *Embo J* **18**, 131-44 (1999).
47. Li, Y., Berke, I., Chen, L. & Jiang, Y. Gating and inward rectifying properties of the MthK K+ channel with and without the gating ring. *J Gen Physiol* **129**, 109-20 (2007).
48. Katz, A.K., Glusker, J.P., Beebe, S.A. & Bock, C.W. Calcium Ion Coordination: A Comparison with That of Beryllium, Magnesium, and Zinc. *J. Am. Chem. Soc.* **118**, 5752-5763 (1996).
49. Pidcock, E. & Moore, G.R. Structural characteristics of protein binding sites for calcium and lanthanide ions. *J Biol Inorg Chem* **6**, 479-89 (2001).
50. Tang, S. et al. Molecular localization of ion selectivity sites within the pore of a human L-type cardiac calcium channel. *J Biol Chem* **268**, 13026-9 (1993).
51. Ellinor, P.T., Yang, J., Sather, W.A., Zhang, J.F. & Tsien, R.W. Ca2+ channel selectivity at a single locus for high-affinity Ca2+ interactions. *Neuron* **15**, 1121-32 (1995).
52. Yang, J., Ellinor, P.T., Sather, W.A., Zhang, J.F. & Tsien, R.W. Molecular determinants of Ca2+ selectivity and ion permeation in L-type Ca2+ channels. *Nature* **366**, 158-61 (1993).
53. Otwinowski, Z. & Minor, W. Processing of X-ray diffraction data collected in oscillation mode. *Methods Enzymol* **276**, 307-326 (1997).
54. Brunger, A.T. et al. Crystallography & NMR system: A new software suite for macromolecular structure determination. *Acta Crystallogr D Biol Crystallogr* **54 (Pt 5)**, 905-21 (1998).
55. Jones, T.A., Zou, J.Y., Cowan, S.W. & Kjeldgaard. Improved methods for building protein models in electron density maps and the location of errors in these models. *Acta Crystallogr A* **47 (Pt 2)**, 110-9 (1991).
56. Heginbotham, L., LeMasurier, M., Kolmakova-Partensky, L. & Miller, C. Single streptomyces lividans K(+) channels: functional asymmetries and sidedness of proton activation. *J Gen Physiol* **114**, 551-60 (1999).
57. Heginbotham, L., Kolmakova-Partensky, L. & Miller, C. Functional reconstitution of a prokaryotic K+ channel. *J Gen Physiol* **111**, 741-9 (1998).
58. Nishida, M., Cadene, M., Chait, B.T. & MacKinnon, R. Crystal structure of a Kir3.1-prokaryotic Kir channel chimera. *Embo J* **26**, 4005-15 (2007).
59. Jin, T. et al. The (beta)gamma subunits of G proteins gate a K(+) channel by pivoted bending of a transmembrane segment. *Mol Cell* **10**, 469-81 (2002).
60. Magidovich, E. & Yifrach, O. Conserved gating hinge in ligand- and voltage-dependent K+ channels. *Biochemistry* **43**, 13242-7 (2004).

61. Zhao, Y., Yarov-Yarovoy, V., Scheuer, T. & Catterall, W.A. A gating hinge in Na+ channels; a molecular switch for electrical signaling. *Neuron* **41**, 859-65 (2004).
62. Ding, S., Ingleby, L., Ahern, C.A. & Horn, R. Investigating the putative glycine hinge in Shaker potassium channel. *J Gen Physiol* **126**, 213-26 (2005).
63. Perozo, E., Cortes, D.M. & Cuello, L.G. Three-dimensional architecture and gating mechanism of a K+ channel studied by EPR spectroscopy. *Nat Struct Biol* **5**, 459-69 (1998).
64. Perozo, E., Cortes, D.M. & Cuello, L.G. Structural rearrangements underlying K+-channel activation gating. *Science* **285**, 73-8 (1999).
65. Liu, Y.S., Sompornpisut, P. & Perozo, E. Structure of the KcsA channel intracellular gate in the open state. *Nat Struct Biol* **8**, 883-7 (2001).
66. Kelly, B.L. & Gross, A. Potassium channel gating observed with site-directed mass tagging. *Nat Struct Biol* **10**, 280-4 (2003).
67. Zimmer, J., Doyle, D.A. & Grossmann, J.G. Structural characterization and pH-induced conformational transition of full-length KcsA. *Biophys J* **90**, 1752-66 (2006).
68. Iwamoto, M. et al. Surface structure and its dynamic rearrangements of the KcsA potassium channel upon gating and tetrabutylammonium blocking. *J Biol Chem* **281**, 28379-86 (2006).
69. Baker, K.A., Tzitzilonis, C., Kwiatkowski, W., Choe, S. & Riek, R. Conformational dynamics of the KcsA potassium channel governs gating properties. *Nat Struct Mol Biol* **14**, 1089-95 (2007).
70. Takeuchi, K., Takahashi, H., Kawano, S. & Shimada, I. Identification and characterization of the slowly exchanging pH-dependent conformational rearrangement in KcsA. *J Biol Chem* **282**, 15179-86 (2007).
71. Shimizu, H. et al. Global twisting motion of single molecular KcsA potassium channel upon gating. *Cell* **132**, 67-78 (2008).
72. Rabenstein, M.D. & Shin, Y.K. Determination of the distance between two spin labels attached to a macromolecule. *Proc Natl Acad Sci U S A* **92**, 8239-43 (1995).
73. Collaborative Computational Project, N. The CCP4 suite: programs for protein crystallography. *Acta Crystallogr D Biol Crystallogr* **50**, 760-763 (1994).
74. Smart, O.S., Goodfellow, J.M. & Wallace, B.A. The pore dimensions of gramicidin A. *Biophys J* **65**, 2455-60 (1993).
75. Humphrey, W., Dalke, A. & Schulten, K. VMD: visual molecular dynamics. *J Mol Graph* **14**, 33-8, 27-8 (1996).

76. Long, S.B., Campbell, E.B. & Mackinnon, R. Crystal Structure of a Mammalian Voltage-Dependent Shaker Family K+ Channel. *Science* (2005).
77. Noskov, S.Y., Berneche, S. & Roux, B. Control of ion selectivity in potassium channels by electrostatic and dynamic properties of carbonyl ligands. *Nature* **431**, 830-4 (2004).
78. Phillips, K., Dauter, Z., Murchie, A.I., Lilley, D.M. & Luisi, B. The crystal structure of a parallel-stranded guanine tetraplex at 0.95 A resolution. *J Mol Biol* **273**, 171-82 (1997).
79. Vora, T., Bisset, D. & Chung, S.H. Conduction of Na+ and K+ through the NaK channel: molecular and Brownian dynamics studies. *Biophys J* **95**, 1600-11 (2008).
80. Noskov, S.Y. & Roux, B. Importance of hydration and dynamics on the selectivity of the KcsA and NaK channels. *J Gen Physiol* **129**, 135-43 (2007).
81. Lewit-Bentley, A. & Rety, S. EF-hand calcium-binding proteins. *Curr Opin Struct Biol* **10**, 637-43 (2000).
82. Neyton, J. & Miller, C. Potassium blocks barium permeation through a calcium-activated potassium channel. *J Gen Physiol* **92**, 549-67 (1988).
83. Neyton, J. & Miller, C. Discrete Ba2+ block as a probe of ion occupancy and pore structure in the high-conductance Ca2+ -activated K+ channel. *J Gen Physiol* **92**, 569-86 (1988).
84. Armstrong, C.M., Swenson, R.P., Jr. & Taylor, S.R. Block of squid axon K channels by internally and externally applied barium ions. *J Gen Physiol* **80**, 663-82 (1982).
85. Armstrong, C.M. & Taylor, S.R. Interaction of barium ions with potassium channels in squid giant axons. *Biophys J* **30**, 473-88 (1980).
86. Zhou, Y. & MacKinnon, R. The occupancy of ions in the K+ selectivity filter: charge balance and coupling of ion binding to a protein conformational change underlie high conduction rates. *J Mol Biol* **333**, 965-75 (2003).
87. Valiyaveetil, F.I., Leonetti, M., Muir, T.W. & Mackinnon, R. Ion selectivity in a semisynthetic K+ channel locked in the conductive conformation. *Science* **314**, 1004-7 (2006).
88. Yeates, T.O. Detecting and overcoming crystal twinning. *Methods Enzymol* **276**, 344-58 (1997).
89. Morais-Cabral, J.H., Zhou, Y. & MacKinnon, R. Energetic optimization of ion conduction rate by the K+ selectivity filter. *Nature* **414**, 37-42 (2001).
90. Kleywegt, G.J. & Jones, T.A. xdlMAPMAN and xdlDATAMAN - programs for reformatting, analysis and manipulation of

biomacromolecular electron-density maps and reflection data sets. *Acta Crystallogr D Biol Crystallogr* **52**, 826-8 (1996).

91. Ashcroft, F.M. *Ion Channels and Disease*, (Academic Press, San Diego, CA, 2000).
92. Long, S.B., Campbell, E.B. & Mackinnon, R. Voltage Sensor of Kv1.2: Structural Basis of Electromechanical Coupling. *Science* (2005).